Spring 1999

Fiber-Optic Coupled Lidar Receiver System to Measure Stratospheric Ozone

David Brent Harper
Old Dominion University

FIBER-OPTIC COUPLED LIDAR RECEIVER SYSTEM TO MEASURE STRATOSPHERIC OZONE

by

David Brent Harper
B.S.E.E. May 1997, Old Dominion University

A Thesis submitted to the faculty of Old Dominion University in Partial Fulfillment of the Requirement for the Degree of

MASTER OF SCIENCE
ELECTRICAL ENGINEERING
OLD DOMINION UNIVERSITY
May 1999

Approved by:

Hani E. Elsayed Ali (Director)

A.N. Dharamsi (Member)

L. Vahala (Member)

ABSTRACT

FIBER-OPTIC COUPLED LIDAR RECEIVER SYSTEM
TO MEASURE STRATOSPHERIC OZONE

David Brent Harper
Old Dominion University, 1999
Director: Dr. Hani Elsayed-Ali

A fiber-optic coupled lidar receiver system was constructed to determine ozone concentrations in the stratosphere. The system was used to make ground-based measurements of lidar returns from a UV DIAL system. A fiber-optic cable was used to couple the light from the receiver telescope to the light detector. Photon counting was implemented as the light detection technique. This technique allowed detection of 301 and 311 nm lidar returns up to 27.5 and 32.5 km respectively. A software application was developed to control the photon counting system and perform real-time data analysis of measured lidar returns. DIAL measurements of stratospheric ozone were obtained from the system up to 24 km.

Co-Directors of Advisory Committee: Dr. Amin Dharamsi
Dr. Linda Vahala

ACKNOWLEDGEMENTS

My research was conducted at NASA Langley Research Center in Hampton, VA. I would like to thank the entire LIDAR APPLICATIONS GROUP at NASA for their never ending support and help that they provided me throughout my research. The experience I obtained at NASA led to my employment as an electronics engineer with the group.

I would also like to thank my friends and family for their support through my many years in college. Without them, none of this would have been possible.

TABLE OF CONTENTS

TABLE OF CONTENTS (cont'd)

LIST OF TABLES

TABLE

LIST OF FIGURES

LIST OF FIGURES (cont'd)

FIGURE PAGE

CHAPTER 1

INTRODUCTION

1.1 OZONE MEASUREMENT

The measurement of ozone in the atmosphere has become increasingly important over the past two decades. Significant increases of ozone concentrations in the lower atmosphere, or troposhpere, and decreases in the upper atmosphere, or stratosphere, have been attributed to man-made causes [1]. High ozone concentrations in the troposphere pose a health hazard to plants and animals and can add to global warming [1]. On the other hand, ozone in the stratosphere serves as a protective barrier against strong ultraviolet (UV) radiation from the sun [2]. Man-made chloroflourocarbons CFC's act as a catalyst with a free oxygen atom and an ozone molecule to produce two oxygen molecules therefore depleting the protective layer of ozone in the stratosphere [3]. The beneficial and harmful effects of ozone require the study of ozone creation and destruction processes in the atmosphere. Therefore, to provide an accurate model of these processes, an ozone lidar system must be able to be used frequently with as large a measurement range as possible [4].

Various methods can be used to measure atmospheric ozone concentrations. These include different airborne and balloon *in situ* measurements, solar occulation satellite techniques, and the use of lasers in lidar (light detection and ranging) systems to probe the atmosphere [4]. Typical *in situ* devices such as weather balloons can only measure within the direct vicinity of the instrument and are therefore used infrequently [4]. Satellites use solar occulation techniques that yield low horizontal and vertical resolution column densities of ozone. Lidar uses lasers to probe the atmosphere and

analyze the backscattered laser energy to yield information such as temperature distributions and molecular densities. Lasers provide a means in which long-range non-intrusive measurements of ozone as a function of altitude can be made with very high vertical resolution. The range of lidar systems extends to tens of kilometers making ground-based measurements of the high altitude stratosphere possible.

1.2 LIDAR

Lidar has been in use since 1963 [5,6] and works on the same principal as ordinary radar. A radar uses a transmitter to send a directed pulse of electromagnetic radiation into a medium such as air. If the pulse encounters an object in the medium then some of the energy is scattered or reflected. A radar receiver collects some of this reflected radiation, which contains information about the object that it has encountered. For example, the delay between the transmission and detection of the reflected signal can be transformed into the distance from the radar transmitter to the object. Also, a moving object causes a frequency shift in the radar pulse. The speed of the object can be calculated from this shift. Lidar is most commonly used for remote sensing of the atmosphere. One common use of lidar is to measure the concentration of different types of molecular species that are present in the atmosphere.

A lidar system for atmospheric studies consists of a pulsed laser source, a telescope receiver to collect returned light, a light detector, and computer for data analysis. Lasers offer the advantage of coherent and collimated sources that allow long range remote sensing with high temporal and spatial resolution [5]. A laser is pulsed into the atmosphere interacting with the molecules and atoms present. A receiver

telescope then collects the backscattered radiation, which in typical configurations is close to the laser source. The receiver telescope focuses the light return onto an optical detector, such as an avalanche photodiode (APD) or a photomultiplier tube (PMT), turns the returned light pulse into an electrical pulse. This detector is connected to other electronics such as amplifiers and filters and then sent to a computer for analysis.

1.3 OZONE Differential Absorption Lidar (DIAL)

Determination of ozone as a function of altitude can be made using a technique called Differential Absorption Lidar (DIAL). In a typical DIAL system, two laser pulses, separated in time and wavelength, are emitted by the laser system. These pulses, one tuned to high ozone absorption (on-line) and the other tuned to a lower absorption (off-line), are transmitted into and then backscattered by the atmosphere creating a return light signal. This signal is received by a telescope, passed through a narrow band filter, and focused onto a photomultiplier detector. When ozone is present in the atmosphere, the on-line signal decay is faster than that of the off-line due to the absorption by ozone in the atmosphere.

The main advantage of the DIAL technique is that the number density of a species such as ozone can be deduced as a function of altitude. If the two lasers are close in wavelength then each laser pulse should undergo the same aerosol and molecular scattering. The main difference between the two pulses should only be the amount of absorption by ozone. If the absorption cross-sections are well known at each wavelength then accurate ozone number densities as a function of altitude can be calculated.

1.4 OZONE DIAL SYSTEM AT NASA LANGLEY RESEARCH CENTER

The Lidar Applications Group at NASA Langley Research Center has been successfully performing airborne DIAL measurements of tropospheric and stratospheric ozone and aerosols since 1980 [7]. Many of the missions over the past eighteen years have been international experiments including missions over rain forests in Brazil during the burning season and missions to the Arctic to study the evolution of the ozone hole [7]. The DIAL system has been continually upgraded over the years improving laser quality, receiver optics, detection electronics, and data analysis to increase the quality, accuracy, and range of atmospheric ozone and aerosol measurements [7].

1.5 RESEARCH GOAL

The goal of this research is to construct and test a complete lidar receiver system to measure stratospheric ozone concentrations. The system includes a fiber-optic coupled lidar telescope to collect the backscattered lidar signal and focus it onto a photomultiplier tube (PMT). Photon counting is used to detect the weak signal return from the high altitude stratosphere. This receiver system will eventually be incorporated into the aircraft based instrument. The characteristics of the telescope including total transmission efficiency and limits of its measurement range will be determined. Also, optimum conditions for use of this telescope with a photon counting system are made. The lidar equation is solved for expected lidar return signals and these predictions are compared to actual lidar returns. Finally, stratospheric ozone concentrations are measured and compared to ozone sonde balloon measurements.

CHAPTER 2

THEORY

This chapter covers the theory, derivation of equations, and a light detection technique used in lidar systems. First, the chapter begins with the derivation of the elastic backscattered lidar equation with emphasis on the effects of the geometry of the receiver telescope. The DIAL equation is then derived to determine the number density of an absorbing atmospheric species. Finally, photon counting and its advantages for lidar signal detection is covered.

2.1 ELASTIC BACKSCATTERED LIDAR EQUATION

The scattering form of the lidar equation yields the expected received power from a laser propagated into the atmosphere and collected by a receiver that is located near the laser system. The intensity variation in a lidar return signal can be used to determine the relative distribution of molecules and aerosols in the atmosphere. When a high density of molecules or aerosols is present, then the laser light is strongly backscattered and attenuated rapidly. This results in a strong initial signal with a fast decay rate. Conversely, when a low number of particles are present, the laser light propagates further into the atmosphere due to the smaller attenuation and scattering effects. The backscattered power received by the system $P_r(\lambda, R)$ is

$$P_r(\lambda, R) = \frac{P_o \cdot A(\lambda, R)}{R^2} \cdot \frac{c \cdot \tau_L}{2} \cdot \beta(\lambda, R) \cdot \exp\left[-2\int_0^R \kappa(\lambda, R) \cdot dR\right] \qquad (2.1)$$

where P_o is the initial power of the laser pulse, $A(\lambda, R)$ is the receiver system function, R is the range from the receiver to the probed volume, c is the speed of light, τ_L is the laser pulse duration, $\beta(\lambda, R)$ is the cross section for scattering in the backward direction, and $k(\lambda, R)$ is the total extinction coefficient that accounts for all scattering and absorption losses. [4,5,6,8].

The receiver system function $A(\lambda, R)$ can become quite complex depending on the geometry of the optics in the receiver system. The system function must account for the transmission of the receiver optics, the spatial distribution of laser energy, and the range dependent overlap of the telescope's field of view (FOV) and the laser beam (see Figure 2.1) [6].

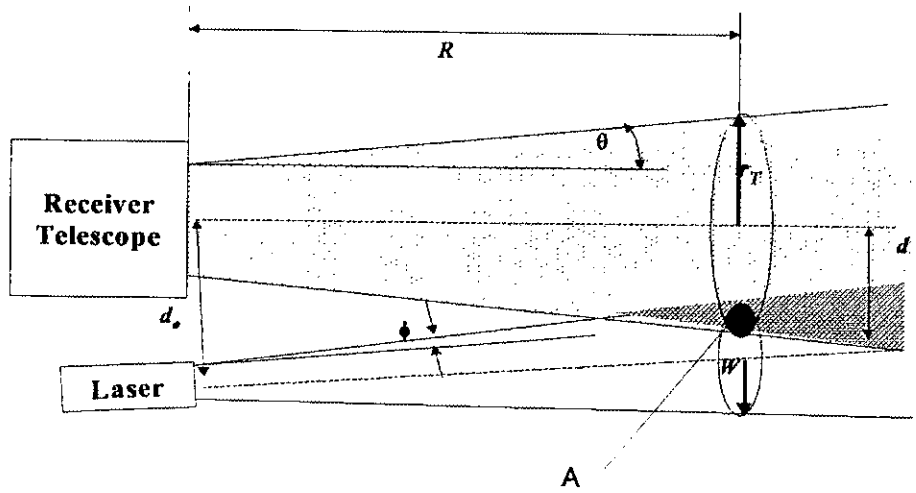

Figure 2.1 Overlap of telescope field of view and laser beam divergence[6].

Most modern lidar systems are monostatic in that the receiver telescope is located near the laser transmitter [6]. In general there are two monostatic arrangements known as *coaxial* and *biaxial*. A *coaxial* arrangement has the telescope field of view axis coincident with the axis of the laser beam. This arrangement allows full overlap of the laser beam and the telescope's field of view at all ranges. In a *biaxial* system, the laser beam enters the field of view at some predetermined range. This arrangement allows discrimination against strong near-field signal returns that may saturate the light detector [4,5,6,7] (see Appendix A).

The system function for a receiver separated by a distant d_o from the laser transmitter then becomes [6]

$$A(\lambda,R) \equiv \frac{\varsigma(\lambda)\cdot A_o}{\pi\cdot W^2(R)} \int_{r=0}^{r_T}\int_{\psi=0}^{2\pi} \xi(R,r,\psi)\cdot F(R,r,\psi)\cdot r\cdot dr\cdot d\psi \quad (2.2)$$

where $\varsigma(\lambda)$ accounts for the transmission of the optics and detector efficiency at wavelength λ, A_o is the area of telescope's primary mirror, *W(R)* is the radius of the laser beam at altitude R, $\xi(R,r,\psi)$ is the probability of backscattered light from point (r,ψ) (polar coordinates) being collected by the receiver, $F(R,r,\psi)$ is the laser energy distribution at point (r,ψ), and r_T is the radius of the telescope's field of view. For a Gaussian laser beam the energy distribution $F(R,r,\psi)$ is

$$F(R,r,\psi)=\exp\left[\frac{r^2+d^2-2\cdot r\cdot d\cdot\cos(\psi)}{W(R)}\right] \qquad (2.3)$$

In a monostatic biaxial system, the telescope FOV partially overlaps the laser beam at some altitudes. The partial overlap of the FOV and the laser at altitude R can be calculated as the intersection of two circles where d is the distance between the laser beam axis and the telescope FOV axis [6]. The probability $\xi(R,r,\psi)$ of the backscattered light being collected can then be described as the area A (see fig.2.1) of this intersection [6]. This overlap function is range dependent with three possible situations occurring.

1. At low altitudes the circles do not overlap, therefore A = 0.
2. At high altitudes, the circles completely overlap and A is equal to the area of the smaller circle, which is usually the laser beam so $A=\pi\cdot W^2(R)$.
3. At middle altitudes, the circles partially overlap. The area A is then equal to the area of the intersection of the two circles [6].

$$A\left(r_T,W,d\right)=W^2\chi_W+r_r^2\chi_r-r_T d\cdot\sin(\chi_r) \qquad (2.4a)$$

where

$$\chi_w=\cos^{-1}\left[\frac{d^2+W^2-r_T^2}{2\cdot r_T\cdot d}\right] \qquad (2.4b)$$

$$\chi_r=\cos^{-1}\left[\frac{d^2+r_T^2-W^2}{2\cdot r_T\cdot d}\right] \qquad (2.4c)$$

Substituting Equations (2.3) and (2.4) into (2.2) may seem to make the integral term too complex, but this integral can be solved quite easily with computers using numerical methods.

2.2 DIFFERENTIAL ABSORPTION LIDAR (DIAL)

Although the relative distribution of molecules and aerosols can be determined from a single lidar return, more accurate techniques can be used to determine the absolute range resolved number density of a species in the probed volume. To determine the number density, the DIAL technique can be used to isolate the absorption effects of a particular molecular species. The DIAL method offers a very sensitive method to remotely measure the number density as a function of altitude.

The DIAL method measures two individual lidar returns that have slightly different wavelengths. One of the wavelengths is tuned to a high absorption line (online) of the species and the other is tuned where less absorption occurs (offline). Since the wavelengths are only slightly different, each signal undergoes the same amount of molecular and aerosol scattering and absorption. The only difference in the return signals should come from the absorption by the species of interest, ozone in the present study. Figure 2.2 shows the absorption cross-section of ozone as a function of wavelength. The online and offline wavelengths transmitted by the NASA UV DIAL system are 301 and 311 nm respectively. This results in absorption cross-sections from Figure 2.2 to be 30×10^{-20} and 9×10^{-20} cm^2 / molec.

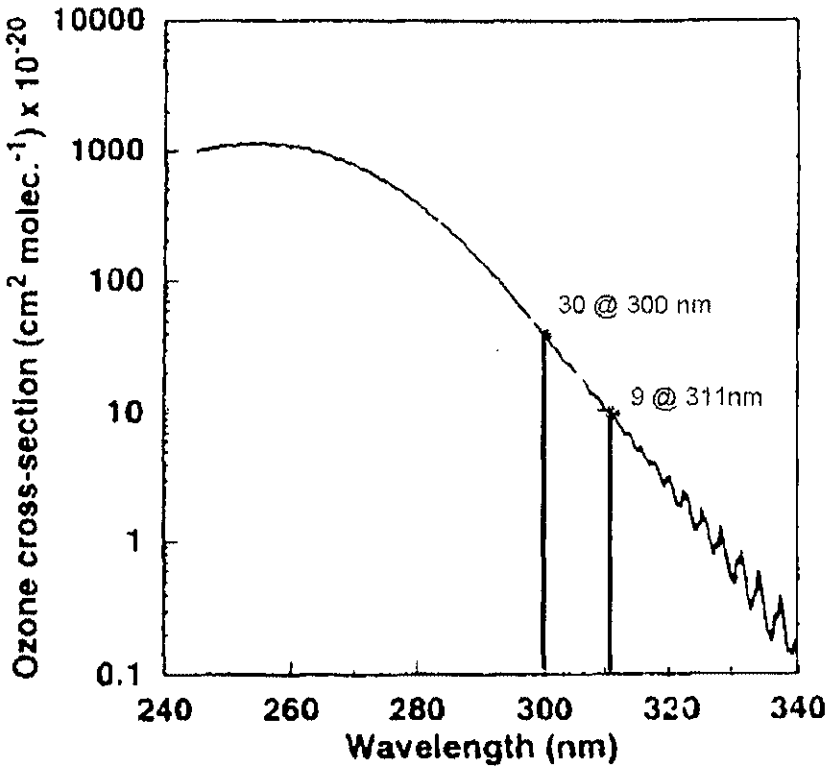

Figure 2.2 Ozone absorption cross-section vs. wavelength. Cross-section values at wavelengths of 301 and 311 nm [1].

The general form of the DIAL equation can be derived by taking the ratio of the return signals. The ratio of the online and offline return signals over a finite range between R_1 and R_2 yields

$$\frac{P(\lambda_{on},R)}{P(\lambda_{off},R)} = \frac{\beta_\pi(\lambda_{on},R)}{\beta_\pi(\lambda_{off},R)} \exp\left[-2\int_0^R \left(\kappa(\lambda_{on},R)-\kappa(\lambda_{off},R)\right)dR\right] \qquad (2.5)$$

The system functions $A(\lambda,R)$ and the $1/R^2$ dependence from each signal cancel out in the ratio leaving the backscatter and total extinction terms [4,6]. The absorption feature of

the species of interest such as ozone can be separated from the total extinction coefficient as

$$\kappa(\lambda, R) = \kappa_a(\lambda, R) + \sigma(\lambda) N(R) \tag{2.6}$$

where κ_a is the absorption and extinction due to aerosols, $\sigma(\lambda)$ is the ozone absorption cross section and *N(R)* is the ozone number density. If the absorption cross sections at the two wavelengths are well known, then we can solve for *N(R)*. Defining the difference in absorption cross sections of the online and offline wavelengths as $\Delta\sigma = \sigma_{on} - \sigma_{off}$, gives the general form of the DIAL equation over a range cell $\Delta R = (R_2 - R_1)$.

$$N(R) = \frac{1}{2 \cdot \Delta\sigma \cdot \Delta R} \cdot \ln\left[\frac{P(\lambda_{off}, R_2) P(\lambda_{on}, R_1)}{P(\lambda_{off}, R_1) P(\lambda_{on}, R2)}\right] \qquad \text{[M]}$$

$$-\frac{1}{2 \cdot \Delta\sigma \cdot \Delta R} \ln\left[\frac{\beta(\lambda_{off}, R_2) \cdot \beta(\lambda_{on}, R_1)}{\beta(\lambda_{off}, R_1) \cdot \beta(\lambda_{on}, R_2)}\right] \qquad \text{[B]}$$

$$-\frac{1}{\Delta\sigma}(\kappa_{on} - \kappa_{off}) \qquad \text{[E]} \tag{2.7}$$

The [M] term yields the more familiar DIAL equation when the [B] and [E] terms are negligible [4,6]. The [B] and [E] terms account for differences in the backscatter and extinction that result from the two different on and off wavelengths. If the difference in wavelength is small, the backscatter is spatially homogeneous, and the sky is relatively clear (high visibility, no clouds), then both terms are small and can be ignored [4]. If we

also assume a negligible error in the absorption cross-section, then the uncertainty in the number density can be written as

$$\delta N^2 = \frac{1}{(2 \cdot \Delta\sigma \cdot \Delta R)^2} \cdot \sum_{\lambda=online}^{offline} \sum_{R=1}^{2} \left(\frac{\partial P}{\partial P(\lambda, R)} \right)^2 \cdot \delta P^2_{(\lambda,R)} \tag{2.8}$$

where $\delta P^2_{(\lambda,R)}$ is the uncertainty in the power of the lidar return signal at wavelength λ and range R [6]. The relative error in the number density ε_N is then

$$\varepsilon_N \equiv \frac{\delta N}{N} = \frac{1}{2 \cdot N \cdot \Delta\sigma \cdot \Delta R} \cdot \sum_{\lambda=online}^{offline} \sum_{R=1}^{2} \left(\frac{\delta P^2_{(\lambda,R)}}{P(\lambda,R)^2} \right)^{1/2} \tag{2.9}$$

The relative error in the DIAL measurement helps to determine the overall measurement range of the system. As the signal-to-noise ratio in the lidar return signal decreases at higher altitudes, the error in the number density increases. If we define an acceptable error in the number density, then the measurement range of the DIAL system can be found at the corresponding altitude of the maximum acceptable error.

2.3 PHOTON COUNTING SYSTEMS

Photon counting is a sensitive light detection technique that can be used in lidar applications. This section begins with the basic operating characteristics of photomultiplier tubes as light detectors used in photon counting systems. The theory of photon counting and the components of a typical system will be discussed. Also, the

different sources of noise and precautions to reduce noise will be covered. Finally, a brief derivation of the signal-to-noise ratio will follow.

2.3.1 *Photomultiplier Tubes(PMT)*

Photomultiplier tubes (PMTs) are very sensitive light detectors. A typical PMT has three major components: a photocathode, a dynode chain, and an anode (see Fig. 2.3). The photocathode is a photosensitive material coated on the internal surface of the PMT that releases electrons when light strikes it. A high negative voltage is placed across the photocathode and dynode chain through a series of resistors. The electrons released from the photocathode are accelerated and focused by the high electric field toward a *CsSb* metal target known as the dynode. The dynode releases many electrons when one electron strikes the surface. These secondary electrons pass through a chain of dynodes amplifying the number of electrons as they hit each dynode. At the end of the chain, the electrical pulse collected by the anode can contain as many as 10^8 electrons [9].

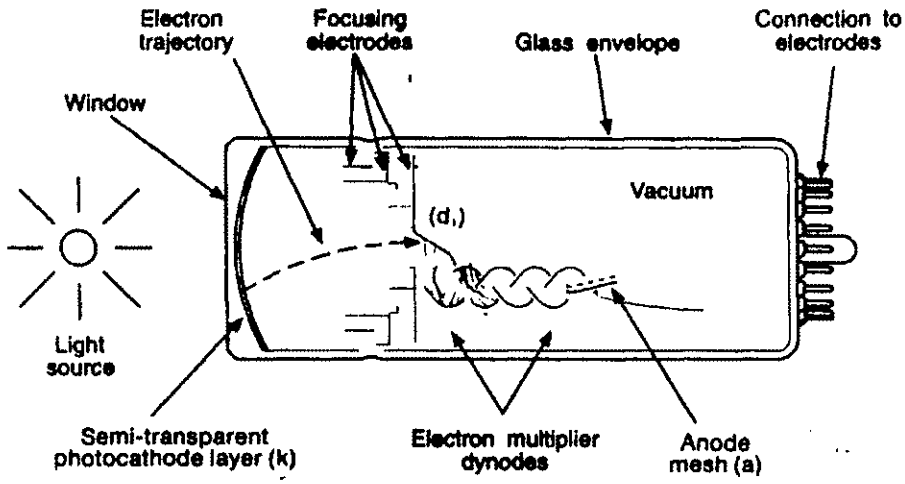

Figure 2.3. Typical photomultiplier tube [9].

Two important characteristics of PMTs are the quantum efficiency (QE) and the gain. The QE describes the number of electrons released for each incident photon. For example, if the QE is 20%, then 20 electrons should be released for every 100 photons incident on the PMT. It is desirable to have as high a QE as possible in order to have a high signal-to-noise ratio. The gain of a PMT is the total number of electrons that arrive at the anode from one electron released from the photocathode. The electron is focused on the first dynode that has a secondary electron emission coefficient of δ. In a chain of n dynodes, the total number of electrons at the anode will be δ^n.

2.3.2 *Photon Counting Theory*

When a photon falls on the photosensitive cathode of the PMT, an electron is released and accelerated toward the first dynode of the dynode chain. The chain increases the number of electrons and a pulse of electrons is collected at the anode. In normal analog detection mode, the anode is connected to a load resistor and the electron

pulses create an average DC current. Typically, the voltage signal across the load resistor is connected to an amplifier and then digitized and averaged for computer analysis. The analog detection method serves as a good detection technique when high light intensities are being measured because of the high signal-to-noise ratio. But, when the light intensity is low, the noise in the system can be higher than the signal putting a limit on the sensitivity of the PMT detector. For DIAL applications, the lowest detectable signal translates into the maximum atmospheric measurement range of the system.

For low light intensity measurements, the discrete nature of the photon can be used. The output pulses at the anode of a PMT are fast (several nanoseconds), separated in time, and discrete. Hence, these fast pulses can be digitally counted instead of measured as an average current. This type of PMT operation is known as single electron response (SER), which describes the PMT's ability to create an electron pulse from a single photoelectron released from the photocathode [9]. Photon counting with this type of PMT operation can offer significant improvements in signal-to-noise ratio compared to analog measurement techniques.

A typical photon counting system, shown in Figure 2.4, consists of a PMT, an amplifier, a pulse height discriminator, and a digital counter. Individual photons from the light source strike the photocathode producing electrical pulses at the anode. The output pulses from the PMT are sent through a high bandwidth amplifier. The amplifier brings the PMT signal to a level compatible with the pulse height discriminator electronics. The pulse height discriminator compares the input signal to an adjustable threshold voltage. All input pulses above this threshold are sent to the output with equal pulse height and width so they can be digitally counted. Any pulses below the set threshold are ignored

and do not get sent to the output. The digital counter is a multi-channel scaler with an averaging memory. Each channel, or bin, stores the number of pulses received from the discriminator during a count time determined by the system clock. For example, for a common clock rate of 1 MHz, each bin stores the number of pulses received in 1 usec.

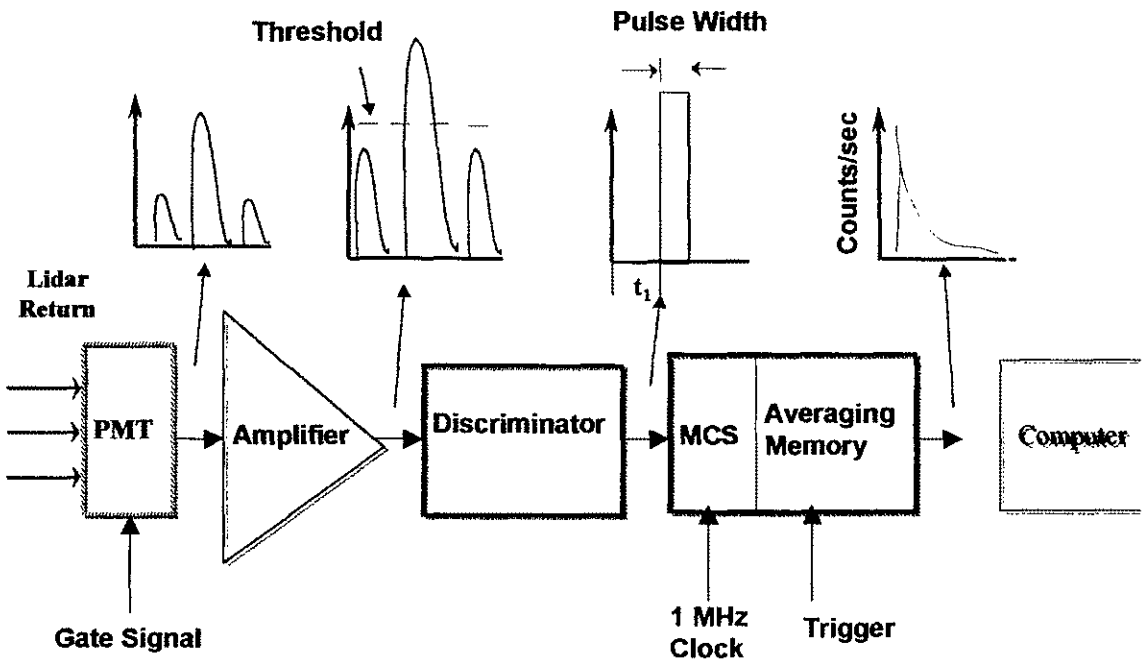

Figure 2.4 A typical photon counting system

The output pulse of electrons at the anode is characterized by its pulse height. The pulse height is determined by the total number of electrons that reach the anode (see Figure 2.5).

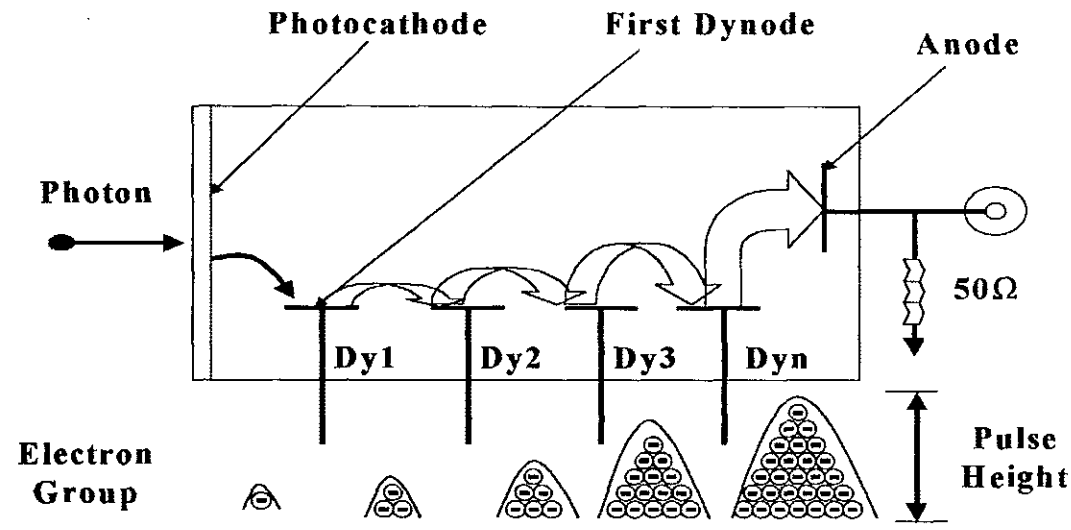

Figure 2.5 Pulse height of electrical output pulse of a PMT [9].

Variations in pulse height result from uncertainties in the secondary electron emission coefficient of the dynodes and the spread in electron trajectories and velocities [9]. Some of the electrons deviate from their normal trajectories and therefore do not participate in the multiplication process. Other variations in pulse height are caused by noise pulses that do not originate from the photocathode. For example, electrons may be emitted from the dynodes by thermionic emission. The pulse height that results from these electrons is smaller because they do not travel through the entire multiplication chain.

The pulse height distribution (PHD) of a typical PMT with and without a light signal applied is shown in Figure 2.6. This PHD shows that the bulk of the noise, which is mostly from dark current, is in the lower pulse height region. The PHD of the applied light signal plus the noise reveals that pulses from the signal to be measured are mainly distributed in a finite region known as the single electron response region.

The optimum measurement point of the PHD is the single electron response peak shown in Figure 2.6. The discriminator is set at this peak to ignore pulses below this point therefore eliminating much of the noise in the output signal [9,10,11].

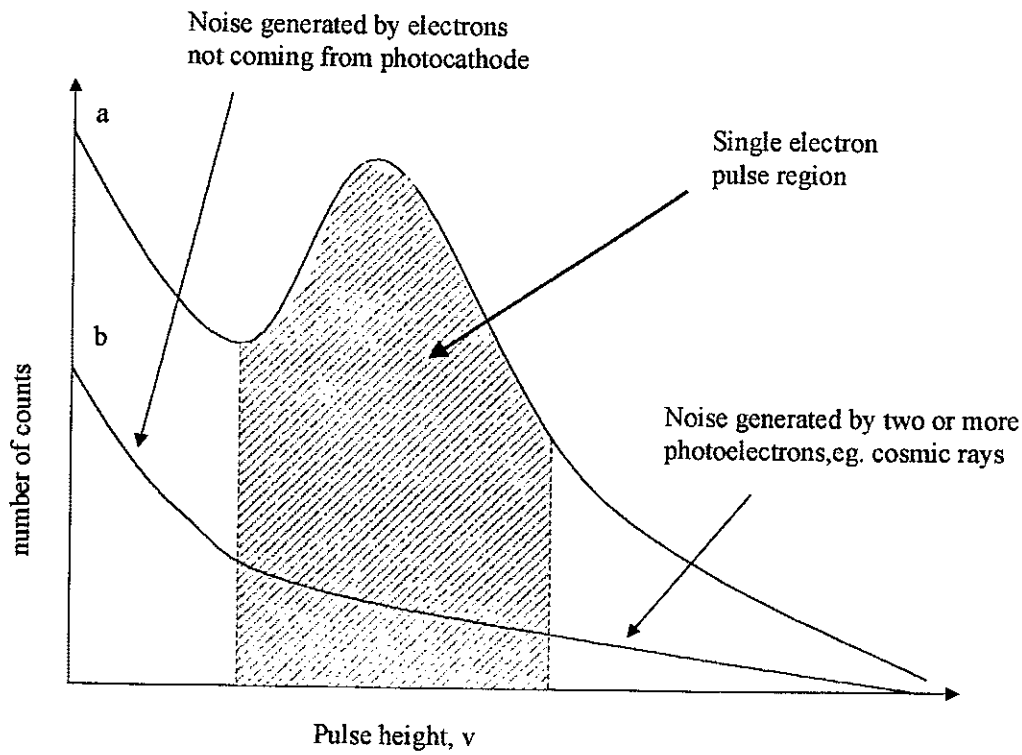

Figure 2.6 Pulse height distribution of a) signal plus noise on a PMT b) PMT noise only [9,10,11].

Good performance of a photon counting system requires that the SER pulses from the PMT remain narrow and that the discriminator is fast enough to respond to each incoming input pulse. The PMT is load matched at 50 ohms with the amplifier to retain the narrow pulse width of the PMT output. The discriminator's ability to respond and recover to be ready for the next pulse is its pulse-pair resolution. A discriminator should have a short pulse-pair resolution in order to reduce pulse pile-up errors. Pulse pile-up happens at high light intensities when photon events occur near the same instance. If the discriminator cannot respond fast enough, these photon events may be counted as one pulse therefore causing an underestimation in the total counts.

2.3.3 Noise in Photon Counting Systems

Several types of noise exist in photon counting systems. These sources of noise come from the non-ideal characteristics of the photomultiplier tubes, background light, and standard electronic noise associated with the accompanying electronics. Each noise component reduces the signal-to-noise ratio, which limits the overall sensitivity of the detector.

The main source of noise in the PMT is called dark current. Dark current is the amount of current that results from electrons that are thermionically emitted by the dynodes and photocathode when no incident light is present. Since the dark current is heavily temperature dependent, maintaining the PMT at a low temperature with liquid or air-cooling can reduce it. Other non-ideal mechanisms occur such as leakage current, glass scintillation, and field emission but are extremely small and can be avoided through proper PMT tube operation and handling precautions. It is usually assumed that the

signal output of a PMT is linearly proportional to the input light intensity and when no light is present there is only the dark current present. While this is a good assumption for low light levels, the PMT output is nonlinear for high input light intensities. Also, when the PMT is exposed to momentary high light intensities, the output does not return to the dark current level immediately but instead decays slowly. This effect is called signal-induced noise (SIN), which can limit the range and accuracy of ozone measurements in a DIAL system [12,13,14,15,16]. Characterization of signal-induced noise effects in DIAL systems can be found in Appendix A.

Depending on the type of application, background light may be a large source of noise in photon counting. In lidar applications, background light from the atmosphere such as sunlight in the daytime or moonlight at night adds a DC baseline to the measured lidar signal. Narrowband optical filters are often used to reduce the background intensity. The remaining background counts can be measured separately when no lidar signal is being pulsed in the atmosphere. In the data analysis, these counts would then be subtracted from the measured lidar return signal counts.

The final noise component in photon counting originates from the electronic components that make up the system. This type of noise is unavoidable but can be reduced in some situations. One of the best ways to reduce electronic noise is by using shielded coaxial cables that limit electromagnetic interference. Also, using cables that are short in length helps reduce electromagnetic interference, pulse broadening, and signal reflections.

The number of pulses that can be counted from a PMT in a given time can be described by Poisson statistics [9,10]. If N_{ph} is the average number of signal pulses, then the standard deviation known as shot noise is

$$n_{ph} = \sqrt{N_{ph}} \tag{2.10}$$

The total number of pulses received at the anode is a combination of pulses from the incident light signal, background light, and dark current. Since N_{ph} cannot be measured separately, it must be calculated by measuring the background and dark current when no signal is present on the PMT and subtracting it from the total signal. The shot noise n_b and n_d from the background light and the dark current are

$$n_b = \sqrt{N_b} \tag{2.11a}$$

$$n_d = \sqrt{N_d} \tag{2.11b}$$

where N_b and N_d are the number of pulses from background and the dark current. Therefore, the total noise in the system n_{tot} can be calculated from each individual noise component as follows:

$$n_{tot}^2 = \left(\sqrt{n_{ph}^2 + n_b^2 + n_d^2}\right)^2 + \left(\sqrt{n_b^2 + n_d^2}\right)^2 \tag{2.12}$$

and substituting $N_{ph} = n_{ph}^2$, $N_b = n_b^2$, and $N_d = n_d^2$

$$n_{tot} = \sqrt{N_{ph} + 2(N_b + N_d)} \tag{2.13}$$

The *SNR* is the ratio of the pulses from the signal to the total noise in the system.

$$SNR = \frac{N_{ph}}{n_{tot}} = \frac{N_{ph}}{\sqrt{N_{ph} + 2\left(N_b + N_d\right)}} \tag{2.14}$$

The *SNR* in Equation 2.13 is a function of the total number of counts measured in a given time [9,10]. To calculate the *SNR* as a function of count rate (counts per second) for a measurement time *t*, we substitute $N'_{ph} = (N_{ph} / t)$, $N'_b = (N_b / t)$, and $N'_d = (N_d / t)$ and the SNR becomes

$$SNR = \frac{N'_{ph}\sqrt{t}}{\sqrt{N'_{ph} + 2\left(N'_b + N'_d\right)}} \tag{2.15}$$

This is the famous result for photon counting. Equation 2.15 shows that the *SNR* for photon counting increases as the square root of the measurement time [9,10]. Long counting times can reveal extremely low signals that would normally be lost using analog detection techniques.

Photon counting offers a very sensitive method to detect low light levels that do not produce analog signals. The discriminator allows the elimination of electronic baseline effects that can cause errors in DIAL calculations. Also, the improvement in the SNR can increase the overall measurement range of a lidar system.

2.3.4 *Photon Counting Form of the Lidar Equation*

The receiver system for this research effort uses photon counting as the light detection technique. The elastic backscattered lidar equation (Eq. 2.1) gives the power collected by a lidar receiver system from a laser pulsed into the atmosphere. This equation can be easily transformed from the power received to the number of photons per second collected. The peak power P_o in the laser pulse is described as

$$P_o = \frac{E_o}{\tau_L} \tag{2.16}$$

where E_o is the energy in the laser pulse and τ_L is the laser pulse width. The number of photons n_λ contained in a laser pulse with energy E_o is

$$n_\lambda = \frac{E_o}{E_p(\lambda)} = \frac{E_o}{\frac{h \cdot c}{\lambda}} \tag{2.17}$$

where $E_p(\lambda)$ is the energy of a photon at wavelength λ, h is Planck's constant, and c is the speed of light. Substituting into Equation (2.1) yields the count rate $C_r(\lambda,R)$ of photons collected by a lidar receiver system.

$$C_r(\lambda,R) = \frac{E_o \cdot \lambda}{h \cdot c \cdot \tau_L} \cdot \frac{A(\lambda,R)}{R^2} \cdot \frac{c \cdot \tau_L}{2} \cdot \beta(\lambda,R) \cdot \exp\left[-2\int_0^R \kappa(\lambda,R) \cdot dR\right] \tag{2.19}$$

The photon counting form of the lidar equation (Eq. 2.19) will be used in Chapter 5 'Results" to calculate predicted lidar signal returns. The backscatter and extinction terms will be obtained from Elterman[17] who has tabulated standard atmospheric attenuation coefficients for lidar applications. The predicted signals will be compared to actual lidar return signals measured with the fiber-optic coupled lidar receiver system. The DIAL equation, neglecting the backscatter and extinction terms, will be used to calculate ozone number densities as a function of altitude from the lidar return signals.

CHAPTER 3

DESIGN AND DEVELOPMENT OF THE FIBER-OPTIC COUPLED LIDAR RECEIVER

This chapter describes the design of a fiber-optic coupled lidar receiver that will be used to measure the ozone concentrations in the stratosphere. The general design of the receiver system is discussed. The influence of each component is then covered to evaluate the performance characteristics. Finally, the total throughput efficiency of the receiver is calculated.

3.1 FIBER-OPTIC COUPLED LIDAR RECEIVER

The type of telescope configuration used in a lidar system depends on the application and cost considerations. Two popular configurations, the Newtonian and Cassegrainian, for lidar receiver telescopes are shown in Figure 3.1 [6].

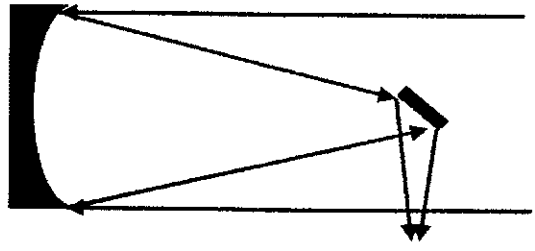

a) Newtonian

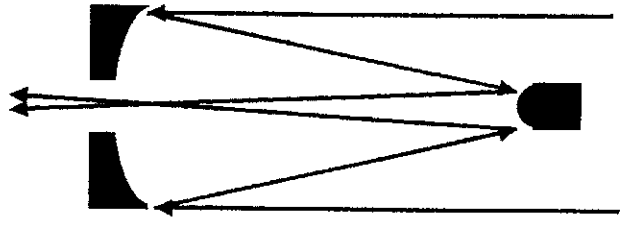

b) Cassegrainian

Figure 3.1. Different receiver telescope configurations commonly used in lidar receivers [6].

The Newtonian configuration was chosen for this research because it offers the best way to couple light into the fiber-optic cable with little loss by obstruction of the primary mirror. Also, it is inexpensive and easy to construct.

The receiver telescope for this research is intended for use with a UV DIAL system that transmits online and offline laser wavelengths of 301 and 311 nm respectively. The purpose of the telescope is to collect as much of the backscattered lidar signal while neglecting as much of the background light as possible. The receiver system is divided into two parts, the telescope with fiber-optic output and the detector package as shown in Figure 3.2.

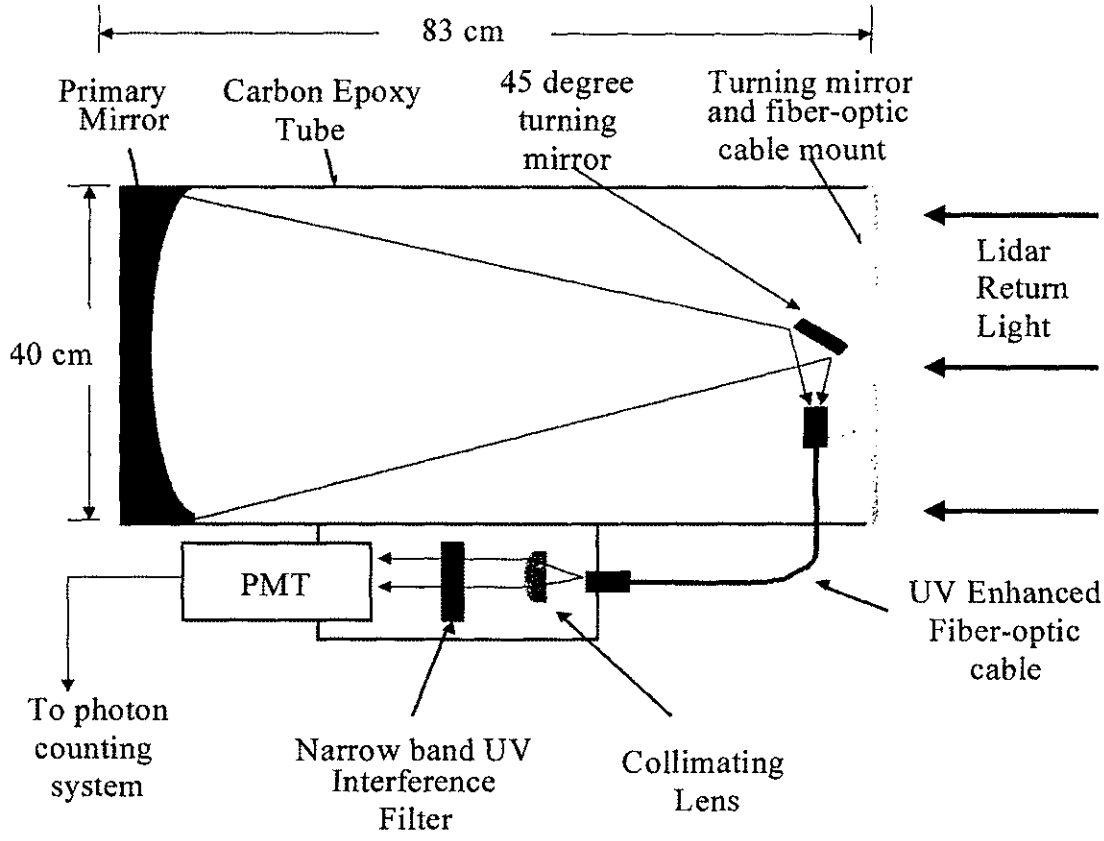

Figure 3.2. Fiber-optic coupled receiver system for stratospheric ozone measurements

The receiver telescope is made up of three optical components: the primary mirror, a small 45-degree turning mirror, and an optical fiber. The components, listed in Table 3.1, are housed in a carbon-epoxy cylinder that is extremely strong and lightweight. The carbon-epoxy has low temperature sensitivity, and therefore does not expand and contract during environmental temperature changes. This helps avoid misalignment of the optics that can occur from material expansion and contraction.

Light reflected from the primary mirror is focused onto the flat turning mirror and then focused onto the core of the optical fiber. With proper design, most of the light collected by the primary mirror can be coupled into the 1-mm diameter fiber-optic cable.

Component	Manufacturer	Properties
Primary Mirror	Desmaris Optical Systems Inc.	Parabolic Mirror 355.6 mm diameter 762 mm focal length aluminum with MgF_2 coating
Turning Mirror	Newport 10D20.RM2	25.4 mm dia. Flat mirror R_{max} = 98% @ 301 nm 45 incidence
Optical Fiber	CeramOptec UV 1000/1060	0.5 meter UV quartz numerical aperture = 0.28 Core diameter = 1 mm

Table 3.1 Optical components of fiber-optic coupled lidar receiver

The purpose of the detector package is to filter and guide the light to the PMT detector. The output of the fiber is connected to the detector package. Light exits the fiber and is collimated by a 25.4-mm diameter plano-convex lens. The collimated light passes through the UV interference filter and strikes the 50.4 mm diameter photocathode of the PMT. The electrical pulses from the PMT are connected to a photon counting system for data acquisition and analysis. Table 3.2 lists the components used in the detector package.

Component	Manufacturer	Properties
Collimating Lens	*Newport* #SPX016.R2	25.4 mm dia. Plano-Convex Focal length = 40 mm
Interference Filter	*BARR* #2290	50% transmission at 301 nm 40% transmission at 311 nm 24 nm FWHM bandwidth
PMT Detector	*Electron Tubes Inc.* Type 9214QB #5150	12 dynode chain linear focused 50.4 mm dia. photocathode QE = 31.5% and Gain @1300 VDC =1.5×10^7

Table 3.2 Components of detector package.

3.2 DESIGN CHARACTERISTICS OF THE RECEIVER

The design characteristics of the receiver telescope require evaluation of its total throughput efficiency and its field of view (FOV). The total throughput efficiency depends upon the size, shape, alignment, and spectral reflectance/transmittance of each

optical component. A high efficiency is desired in order to have a long ozone measurement range. The telescope FOV determines how much of the backscattered lidar signal is collected. The FOV of the telescope should be large enough to collect the backscattered laser signal but small enough to neglect unwanted atmospheric background light [18].

3.2.1 *Primary Mirror*

The primary mirror is the main optical element in the telescope receiver. The diameter, reflectance, and focal spot size determine how much of the lidar signal is collected and coupled into the fiber-optic cable. The amount of signal collected increases as the square of the diameter for the mirror. The primary mirror for the fiber-optic coupled receiver has a diameter of 35.5 cm and is coated with a standard MgF_2 plus aluminum coating for high reflection (90%) at UV wavelengths. The fiber-optic cable and the turning mirror are mounted on a 1.225 cm wide aluminum bar that transverses the diameter of the telescope. The total area of the mount blocking the primary mirror is 35.5 cm^2. The area of the primary mirror is 993.1 cm^2, therefore the total amount of light that will reach the primary is

$$T_{mount} = \frac{993.1 - 35.5}{993.1} \times 100 = 96.4\% \tag{3.1}$$

Light reflected from the primary mirror is focused to a finite spot size. The minimum diameter of the spot size of a mirror is its diffraction-limited spot size [19].

The focal point of a uniformly illuminated mirror has a minimum spot size diameter d_s described by

$$d_s = \frac{2 \cdot f_M \cdot \lambda}{d_M} \tag{3.2}$$

where f_M and d_M are the focal length and diameter of the mirror respectively [19]. Therefore, at 301 nm, the primary mirror from Table 3.1 will have a diffraction limited spot size diameter of 1.28 um, which is approximately 800 times less than the 1 mm core diameter of the fiber-optic cable.

3.2.2 *Fiber-Optic Cable*

Light from the primary mirror is turned by the 45-degree mirror and focused onto the fiber-optic cable. The main goal in the design and construction of this receiver system was to obtain the highest efficiency of light transmission and signal-to-noise ratio as possible. To achieve high efficiency, the receiver should contain as few optical components as possible to reduce losses to reflection, absorption, and scattering. This also reduces difficulties in alignment that is associated with using multiple optic mirrors and lens. The fiber-optic cable provides an easy means to guide the collected light from the telescope to the detector that is usually accomplished by using multiple optics. This section gives a brief description of optical fibers as waveguides and the loss mechanisms that occur.

An optical fiber is a cylindrical waveguide that is made up of low loss glass materials. The central part of the fiber is known as the core and the region surrounding

the core is called the cladding. The core and cladding provide the lightwave guiding feature of the fiber. If light enters the fiber at the proper acceptance angle, determined by the indices of refraction, then the light can propagate in the core through the length of the fiber by total reflection at the core-cladding boundary without losing energy to refraction into the cladding.

For a wave to propagate into a waveguide it must undergo total internal reflection at the waveguide core-cladding boundary [20]. A wave in a medium with refractive index of n_1, incident on a boundary to another medium with refractive index n_2, is partially reflected in medium 1 and partially transmitted in medium 2. The angle of transmitted light into medium 2 can be found from Snell's law.

$$n_1 \sin(\theta_1) = n_2 \sin(\theta_2) \tag{3.3}$$

If n_1 is less than n_2, and the angle of incidence of the wave is greater than some critical angle, then the wave will be totally reflected into medium 1, the core [20,21]. The critical angle is the maximum angle that light in medium 1 can intercept medium 2 and be totally reflected is given by

$$\theta_c = \sin^{-1}\left(\frac{n_2}{n_1}\right) \tag{3.4}$$

Once the condition for total internal reflection is met, light can propagate in the fiber with very little loss. The lightwaves travel through the fiber with different transverse spatial distributions known as modes [20,21,22]. The core and cladding characteristics determine the number of modes that can be supported by the fiber. It can

be shown that higher order modes have larger divergence angles and travel longer distances through the fiber [20,22]. The lower order modes travel closer to the propagation axis and therefore travel shorter distances. This effect is known as modal dispersion. Modal dispersion consequently causes a spreading of the pulse width. This effect is negligible for the fiber in this research due to its short length. [20].

To efficiently couple light into a fiber, the incident light must enter within the acceptance angle of the fiber. The acceptance angle is defined as the maximum angle in which light can enter the core of the fiber and still propagate by internal reflection through the fiber. A lightwave in air (refractive index $n_o \cong 1$), incident on a fiber at angle θ refracts into the core. If the angle of the refracted light into the core is less than the critical angle when it strikes the core-cladding boundary, then the light will undergo total internal reflection (see Figure 3.3). The acceptance angle can be found by deriving the angles of refraction governed by Snell's law [20,21,22]. A constant known as the numerical aperture (*NA*) relates the indices of refraction of the core and cladding of the fiber. The maximum acceptance angle α_{acc} of a fiber can then be calculated as

$$\alpha_{acc} = \sin^{-1}(NA) \tag{3.5}$$

where

$$NA = \sqrt{(n_1^2 - n_2^2)} \tag{3.6}$$

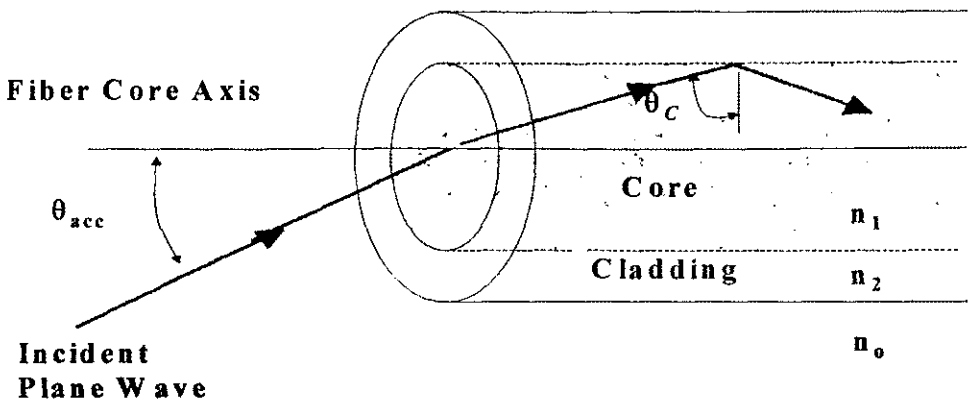

Figure 3.3 Acceptance angle of an optical fiber [20].

The fiber from Table 3.1 with a $NA = 0.28$ has an acceptance angle of 16.26°, which is greater than the 13.8° mirror illumination angle θ_{inc} as shown in Figure 3.4.

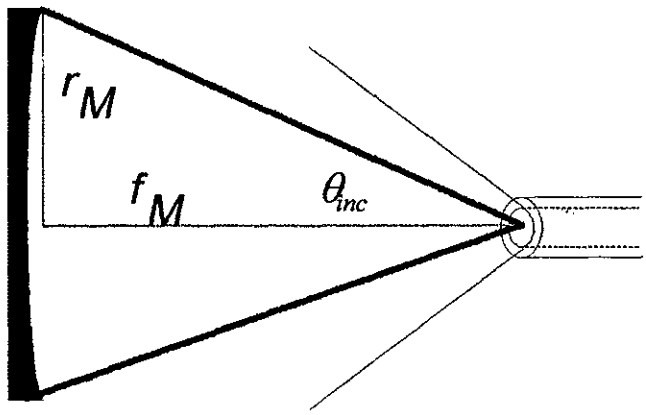

$$\theta_{inc} = \tan^{-1}\left(\frac{r_M}{f_M}\right) = \tan^{-1}\left(\frac{177.8}{762}\right) = 13.8°$$

Figure 3.4 Angle of incident light on fiber.

Therefore, all the light from the mirror should be coupled into the fiber except for a small percentage that is reflected at the air-fiber boundary (4%). This reflection loss is calculated from standard electromagnetic theory using Snell's law . If the fiber end is not antireflection coated, then the reflection coefficient at the boundary is $R \approx 4\%$ yielding a total coupling efficiency into the fiber of 96%.

Once light is launched into the fiber, the light is guided to the output subject to losses in the fiber. There are three different types of loss mechanisms in optical fibers; the first is from bending of the fiber, the second is from scattering losses, and third is losses due to absorption [20,22]. It is fairly obvious why bends in fibers should give rise to losses. To maintain a wavefront that is perpendicular to the direction of propagation when the fiber is bent, the part of the wave that is close to the core-cladding boundary must travel faster than the part near the center of the core. In theory, each mode extends infinitely into the cladding even though the electric field decreases exponentially as it projects into the cladding. That would mean when there is a bend in the fiber, the extended light on the outside of the bend would have to travel faster than the light at the inside of the bend in order to maintain a uniform wavefront. If that were the case, the outer part of the wavefront would have to travel faster than the speed of light to keep up, which according to relativistic theory is not possible. Therefore, the light not contained in the core will be lost to radiation (heat) from the core. Fibers with bends of small radii of curvature will cause higher order modes that are propagating in the fiber to incur the greatest loss [20].

The main losses resulting from the physical structure of the fiber are scattering losses and absorption losses. The scattering losses occur from the non-ideal chemical

structure of the fiber. The chemical composition can vary from place to place throughout the fiber. This type of non-ideal chemical composition can cause differences in the refractive indices of the material. If these differences are on the order of the wavelength divided by ten or more, then these fluctuations can act as Rayleigh scattering points. The Rayleigh scattering coefficient is proportional to $1/\lambda^4$ and is the cause of most of the attenuation at shorter wavelengths [22]. To reduce the loss at UV wavelengths by Rayleigh scattering, materials such as UV grade fused silica must be used.

Losses in the longer wavelengths result from two absorption processes in the fiber material. The first process is a result of the transitions between lattice vibrational states. These transitions correspond to the infrared region from about 1600nm and above. Impurities in the fiber material are the other source of attenuation. Often, the wavelength of the transmitted light corresponds to a peak absorption wavelength of the impurity. One of the largest contributors of this type of loss is the presence of hydroxyl ions (OH^-). The major advances in decreasing the attenuation in fiber optics over the years have come from the effective control over the densities of impurities during the manufacturing process [20].

The fiber used in this research effort (Table 3.1) is made of UV grade fused silica (quartz) that has a high transmission at UV wavelengths with about 1% loss at 301 nm. The coupling efficiency, loss by reflection at each end, and the transmission of the fiber yield a high total throughput efficiency of the fiber to be 91%. Therefore, less than 10% of the total signal should be lost using the fiber-optic cable to guide the signal to the detector package.

3.2.3 *Detector Package*

Optimum performance of the entire receiver requires that the filter passes only the desired wavelengths and that all of this light strikes the photocathode of the PMT. Interference filters are best suited for UV wavelengths because of their high UV transmission. Since the spectral transmission of interference filters is dependent on the incident angle, the light from the output of the fiber must be collimated before being passed through the filter.

The collimating lens has a diameter of 25.4 mm and is anti-reflection coated to provide > 99% transmission at 301 nm. The fiber is placed at the focal length of the lens to collimate the light exiting the fiber. The spectral transmission of the interference filter was measured at the NASA Langley spectroscopy lab with a Cary-14 spectrophotometer. The UV interference filter has a total bandwidth of 24 nm FWHM from 288 to 312 nm. The transmission at the laser wavelengths 301 and 311 nm is 50% and 40% respectively.

The collimated light passes through the filter and strikes the photocathode of the PMT. The diameter of the photocathode is 50.4 mm, therefore all of the collimated light that is passed through the filter strikes the photocathode. The PMT used in this research effort was an *ETI* 9214Q. This PMT was suggested for DIAL applications by Eccles[23] based on its high QE at 301 nm (31.5%) and its high gain (1.5×10^7) at low operating voltage of -1300 VDC (see Appendix C).

3.2.4 *Telescope FOV and Total Throughput Efficiency*

The FOV of the telescope is limited by the size of the field stop aperture. In the case of the fiber-optic coupled receiver, the core of the fiber is the field stop. At short ranges, the FOV of each point of the mirror is slightly different [6]. This effect decreases for longer ranges and can be ignored for this receiver. The application of this receiver system is to measure upper atmospheric (stratosphere) ozone. At these high altitudes, the full angle FOV can be estimated as

$$\theta_{FOV} = \frac{d_f}{f_M} \tag{3.6}$$

where d_f is the field stop diameter and f_M is the focal length of the primary mirror [6]. The FOV of a telescope should be large enough to collect all the backscattered radiation while minimizing the amount of background light collected. For maximum signal-to-noise ratio, the FOV of a receiver (depending on the application) should be between 1.0 and 2.0 times the divergence of the laser beam [18]. The lasers for NASA Langley's UV DIAL system typically have divergences between 0.5 and 1 mrad [7]. The FOV of the fiber-optic coupled lidar receiver, with the 762-mm focal length primary mirror and 1-mm diameter fiber core, is 1.3 mrad. This FOV is within the constraints defined in the Lidar Technical Notes [18].

The total throughput efficiency of the receiver telescope to the PMT photocathode can be calculated from the individual spectral characteristics of each part of the system. The total efficiency is then

$$\varepsilon(\lambda) = T_{mount} \cdot R_{M1}(\lambda) \cdot R_{M2}(\lambda) \cdot C_{fiber} \cdot T_f(\lambda) \cdot T_{Coll} \cdot T_{IF} \tag{3.7}$$

where T_{mount} is the transmission of the light with the cable and turning mirror mount blocking the primary, $R_{M1}(\lambda)$ is the reflectivity of the primary mirror, $R_{M2}(\lambda)$ is the reflectivity of the turning mirror C_{fiber} is the coupling efficiency of light into the fiber, $T_f(\lambda)$ is the transmission of the fiber, $T_{Coll}(\lambda)$ is the transmission of the collimating lens, and $T_{IF}(\lambda)$ is the transmission of the interference filter at wavelength λ. Therefore, the expected total throughput efficiency for the fiber-optic coupled lidar receiver to the PMT detector is

$$\varepsilon(\lambda) = 38.4\% @ 301\ nm$$

$$\varepsilon(\lambda) = 30.7\% @ 311\ nm$$

The total efficiency of the telescope receiver calculated above does not include the QE efficiency of the PMT detector. We can solve for the system transmission coefficient $\xi(\lambda)$ in the photon counting form of the lidar equation by multiplying QE of the detector by the total throughput efficiency. If we assume that all electron pulses produced by incident photons are counted, then the system transmission coefficient $\varsigma(\lambda)$ is

$$\varsigma(\lambda) = \varepsilon(\lambda) \cdot QE \tag{3.8}$$

The performance characteristics of the entire receiver system are expected to yield a high signal-to-noise ratio. This system has a high transmission at the laser wavelengths

of 301 and 311 nm, and a low transmission at wavelengths above and below this region. The above characteristics should allow all the backscattered laser energy, where there is full overlap of the FOV and laser beam, to be collected while neglecting much of the background light that may be present.

CHAPTER 4

EXPERIMENTAL SETUP

The following chapter describes the experimental setups for measuring the spectral transmission characteristics of the telescope and detector package. The current ozone DIAL system at NASA Langley Research center is also described. Finally, the experimental setup for using the fiber-optic coupled receiver system to make ground based stratospheric ozone measurements is discussed.

4.1 SPECTRAL TRANSMISSION CHARACTERISTISCS OF RECEIVER SYSTEM

The performance of the fiber-optic coupled telescope depends upon the optics that make up the receiver. The spectral characteristics of each optical component must be measured in order to determine the expected signal-to-noise ratio of the system. High signal-to-noise ratio translates into long atmospheric measurement ranges, which is desired for remote sensing of ozone in the high altitude stratosphere.

In the experimental setup, a collimated light source was used as shown in Figure 4.1. A 1000-W Xe continuous wave lamp placed in an air-cooled housing provided an intense UV light spectrum. The lamp was powered by an adjustable DC power supply that has an optical feedback amplifier coupled into the lamp housing. The feedback amplifier provides lamp stability to under 0.1% ripple. A high intensity grating monochromator was used to select the desired wavelengths from the Xe lamp. Light from the monochromator was coupled into a UV enhanced quartz fiber with 1 mm core diameter. The output of the fiber acted as a point source that was placed at the focal point of a

collimating mirror. An adjustable iris was placed at the output of the fiber to control the diameter of the illumination circle on the collimating mirror. The cone of light exiting the fiber was collimated into a parallel beam that was reflected into the fiber-optic telescope designed in this research effort.

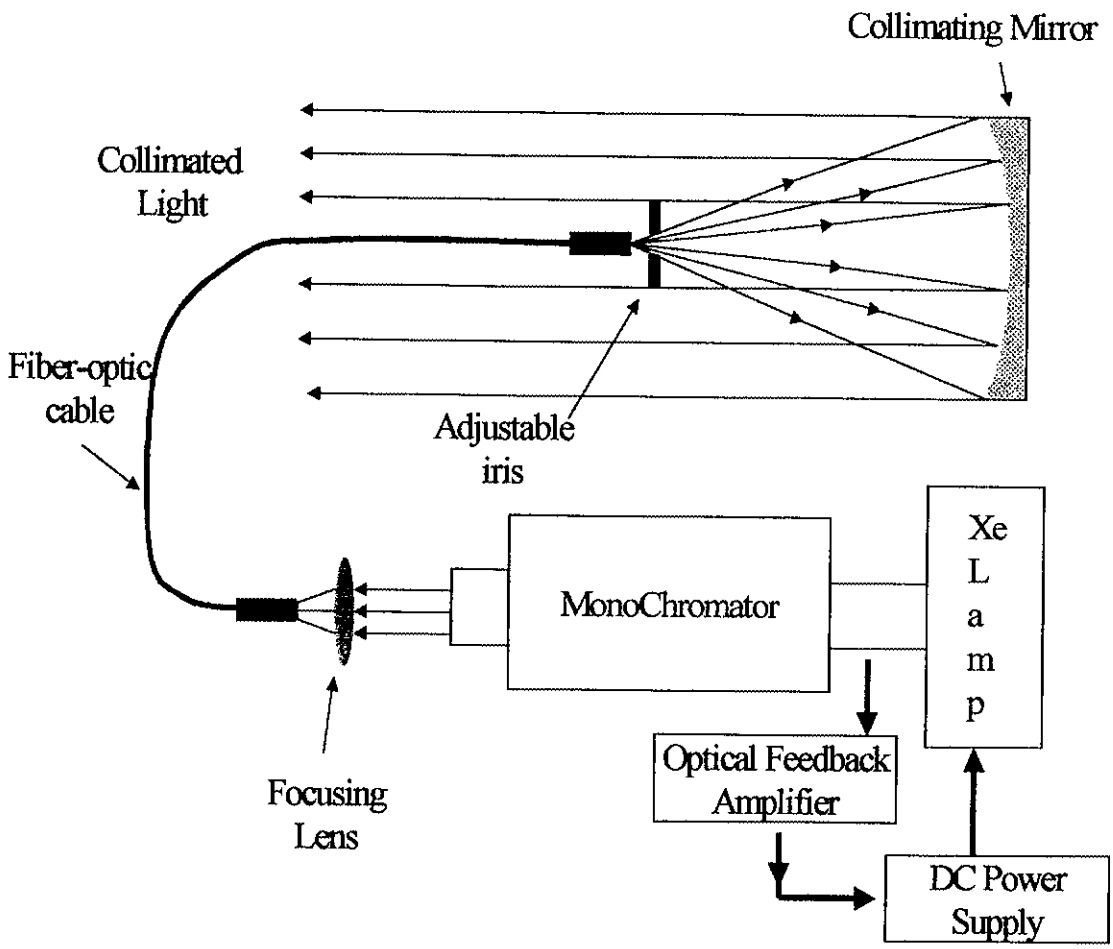

Figure 4.1. Collimated light source for measuring spectral characteristics of receiver optical elements.

The spectral response of the telescope primary mirror, turning mirror, and fiber were measured by placing a standard UV PIN diode detector at each point as shown in Figure 4.2. The current from the detector was measured with a picoammeter. The reflectivity or transmission of each element was determined by taking the ratio of the measured reflected/transmitted light and the measured incident light.

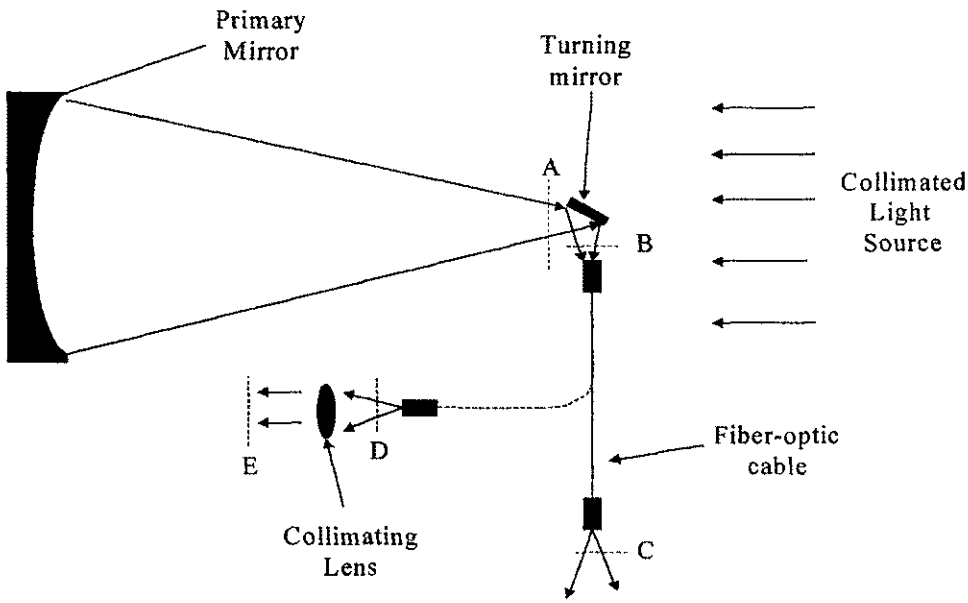

Figure 4.2 Measurement points A,B,C,D and E for spectral transmission and reflection of each optical element.

The collimated light source strikes the primary mirror, which focuses the light to a finite spotsize at its focal length. The PIN diode detector was first placed at the output of the light source fiber (see Figure 4.1) to measure the incident light on the telescope. This measurement was multiplied by the reflectivity of the collimating mirror in order to calculate the incident light striking the primary mirror. The detector was then placed at point *A* near the turning mirror. In order to make as accurate measurement as possible,

the full area of the detector was used. The detector was then placed at point *B* to measure the reflectivity of the turning mirror. The measurements from point *A* were used as the incident light on the turning mirror.

The coupling efficiency and the absorption of the fiber were measured by taking the ratio of the output and input light intensities at points *B* and *C* respectively. This ratio yielded the coupling efficiency of the fiber that includes the amount of light coupled into the fiber with losses by reflection at the endpoints and absorption and scattering losses as the light travels through the fiber.

The previous measurement did not include losses due to the bending of the fiber. The fiber in the configuration for this receiver telescope has one 90-degree bend with a radius of curvature of 17.1 cm. The measurement of the output of the fiber with the bend at point *D* divided by that of the measurement without the bend at point *C* is the amount of bending loss. Losses from multiple bends in the fiber were not measured because the configuration of the telescope requires only one bend in the fiber before the output is placed into the detector package.

Since the spectral characteristics of the interference filter and the PMT are known (see Ch 3.2.3), the collimating lens is the only component in the detector package to be measured. The transmission of the collimating lens was measured by taking the ratio of the incident light measured at point *D* and the transmitted light at point *E*. The area of the PIN diode detector is only 3 cm^2 so the fiber was placed a few centimeters off of the focal point. This created an illumination circle that could be measured by the full area of the PIN diode detector.

4.2 STRATOSPHERIC OZONE MEASUREMENT SYSTEM SETUP

4.2.1 *Ozone DIAL Laser System*

The current ozone DIAL laser system at NASA Langley Research Center, shown in Figure 4.3, consists of two types of lasers to produce the online and offline wavelengths. Two high-power *Continuum* Nd:YAG lasers are frequency-doubled, which then pump dye lasers. The dye lasers are doubled to produce 289 and 299 nm for tropospheric measurements or 301 and 311 nm for stratospheric measurements. These lasers operate at a repetition rate of 30 Hz. The output power depending on the type of dye used is between 10 and 30 mJ per pulse. The laser beams are transmitted in the zenith for ground based measurements through a door in the building roof [7].

The DIAL system has two 35.5 cm diameter Cassegrainian telescopes to collect the returned light backscattered from the atmosphere from the zenith and nadir directions. Each optical surface is protected with a triple-band anti-reflection coating to reduce losses of the light passing through the receiver optics [7].

Photomultiplier tubes (PMTs) are used in an analog configuration for light detection. A 5 MHz analog-to-digital converter (ADC) connected to a computer stores an average of a variable number of lidar returns. The 5 MHz ADC allows a 30-meter atmospheric measurement resolution [7].

The ozone DIAL system was used as the laser transmitter source for this research. The fiber-optic coupled lidar receiver using photon counting was used to measure the backscattered lidar returns from the transmitted online and offline laser pulses. No measurements were made by the NASA analog system because the beams were aligned to the fiber-optic coupled receiver telescope.

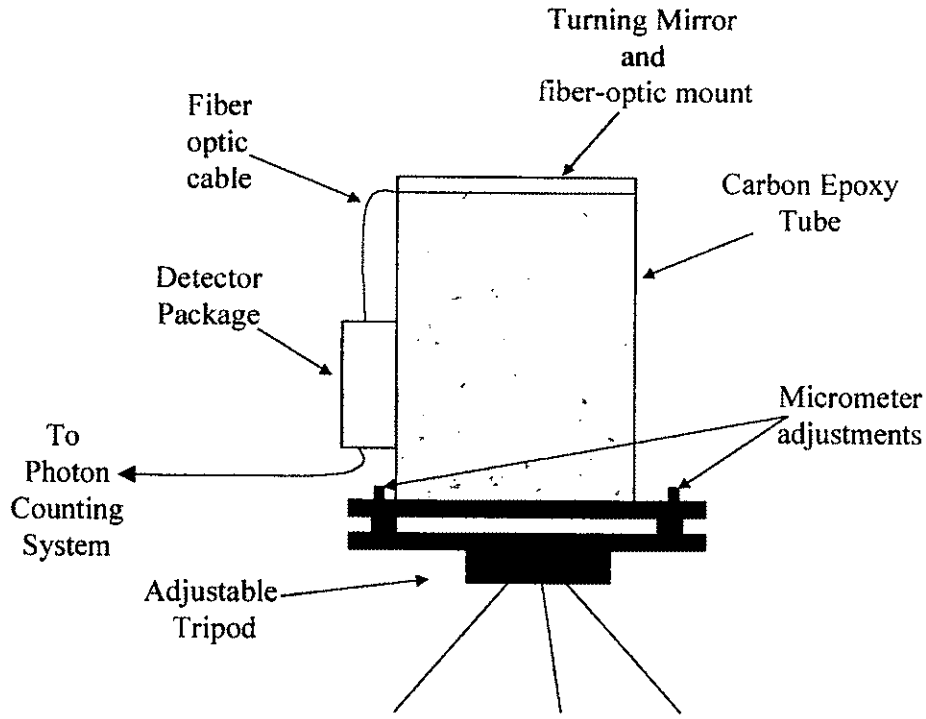

Figure 4.4. Fiber-optic coupled receiver system. Receiver is mounted on an adjustable tripod for telescope alignment

The fiber-optic coupled lidar receiver was placed approximately one meter away from the exit of the laser beams on an adjustable tripod (see Figure 4.3). The micrometers allowed for additional adjustments that were sometimes needed to align the telescope and laser beams. This *biaxial* arrangement allowed discrimination against strong near-field returns that saturate the PMT detector. The return signals were maximized by monitoring the output from the PMT anode on an oscilloscope. After the telescope and the lasers were aligned, the anode of the PMT was connected to the photon counting system to measure the backscattered lidar returns (see Fig. 4.5).

The photon counting system used in this research effort is shown in Figure 4.5. Although the receiver telescope was placed one meter away from the lasers, some of the strong near-field signal was still in the FOV of the telescope. Therefore, the PMT is gated with the circuit in Appendix C to avoid saturation.

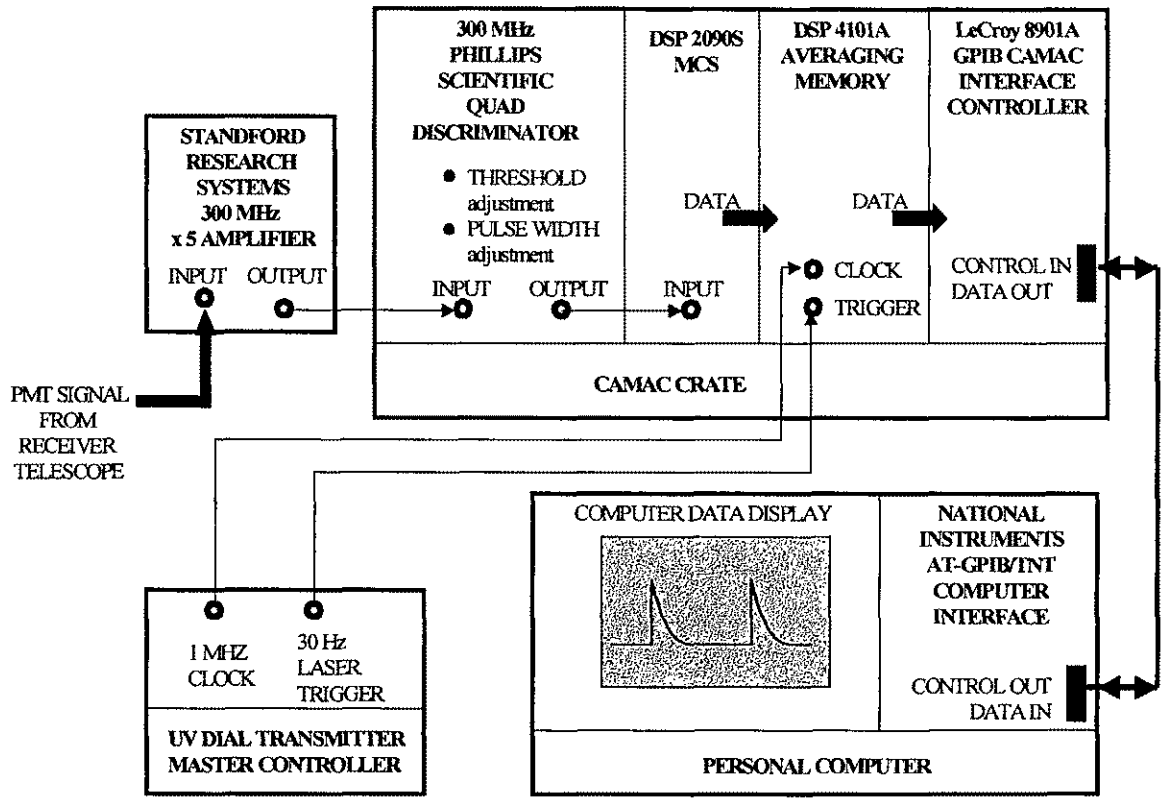

Figure 4.5 Photon counting system setup.

Signal pulses from the PMT were sent to a Standford Research Systems 300 MHz amplifier with a gain of 5. The amplifier has an input impedance of 50 ohms so the PMT is properly load matched. The amplified pulses were then passed through a 300 MHz Phillips Scientific 704 Quad discriminator. The discriminator has a variable threshold setting from -10 mV to -1 V and a variable output pulse width that ranges from 2 nsec to 50 nsec. The input pulses above the set threshold were sent to a DSP 2090S multichannel-scaler (MCS). When the MCS receives a trigger signal, it counts the number of pulses received from the discriminator and stores the number into time bins. The counting time for each bin is set by the clock rate. A 1 MHz clock rate yields a count time of 1 usec per bin. The number of pulses in each bin is stored in a DSP 4101A averaging memory. The 1 MHz clock and 30 Hz laser trigger were provided by the NASA UV DIAL Transmitter Master Controller.

The optimum operating conditions for these components in the photon counting system were determined in previous research by Eccles[23]. His research suggested that the PMT in Table 4.1 be operated at a voltage of -1300 VDC with a dynode gating circuit for maximum linear signal response. Eccles[23] also concluded that the discriminator output pulse width should be set to 5 nsec and the discriminator threshold be set to about 110 mV (see Appendix C).

The discriminator, MCS, and averaging memory are mounted in a standard CAMAC crate. A LeCroy 8901A GPIB CAMAC crate controller allows computer interface with the mounted components. A computer with a National Instruments AT-GPIB/TNT interface allows control and data acquisition processes with the CAMAC crate.

4.2.3 *Computer Software for Photon Counting System*

A software program was developed in Microsoft™ VISUAL C++ to control and acquire data from the photon counting system. The program is a 32-bit WINDOWS™ application that provides ease of operation and a user-friendly environment to control the photon counting system. The program records setup information from the user including laser repetition rate, laser pulse width, discriminator threshold voltage, discriminator output pulse width, and PMT operating voltage. The program sets the number of bins and the total photon counting time to accumulate data. After the total counting time has expired, the data from the averaging memory is read into the computer through the GPIB communication interface. The setup information and the data are recorded into individual files and displayed on the screen monitor. The program also includes a DIAL calculation feature that determines real time ozone concentrations as a function of altitude from the data acquired. For post data analysis, the program also converts the photon counting data files into text files that can be read by standard spreadsheet and mathematical software applications.

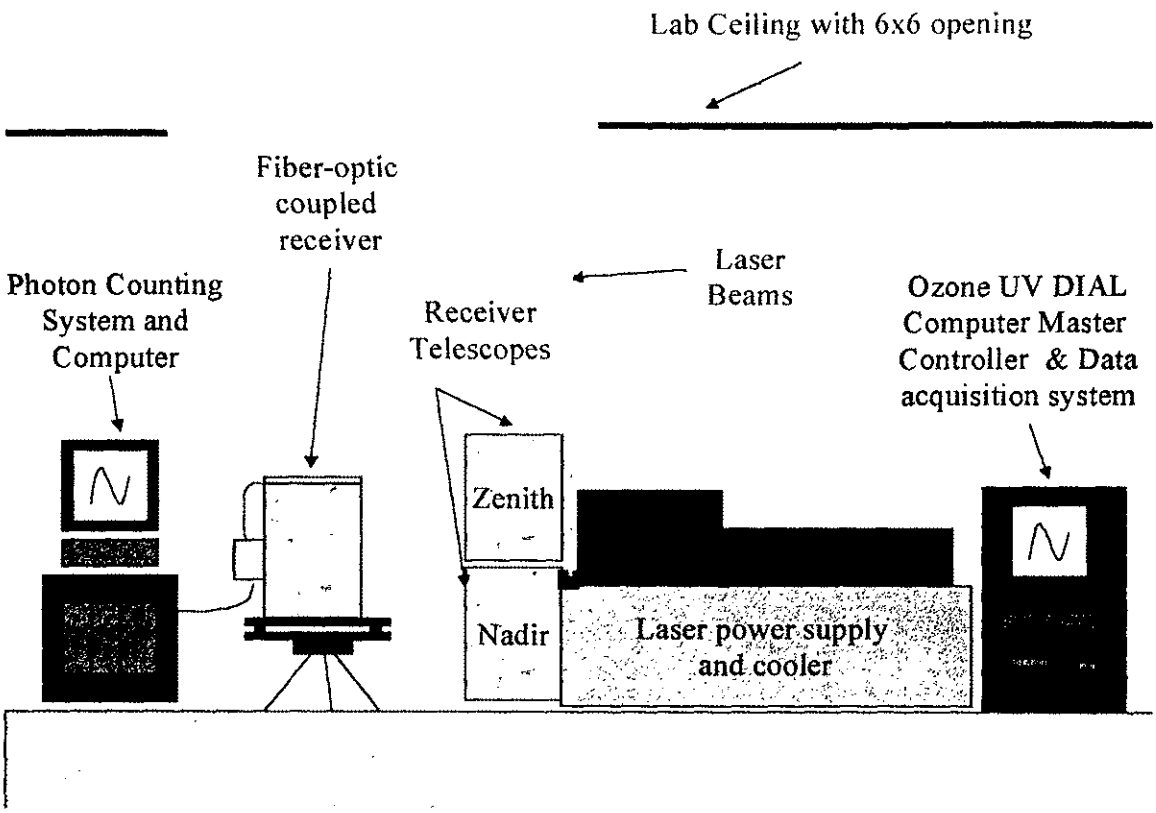

Figure 4.3. Current ozone UV DIAL system in ground test lab. Fiber-optic coupled receiver system placed one meter away from lasers (drawing not to scale).

4.2.2 *Fiber-optic coupled receiver system*

Stratospheric ozone measurements were made using the fiber-optic coupled receiver shown in Figure 4.4. The receiver system was connected to the photon counting system to measure the backscattered lidar signals from the online and offline lasers. Data from the photon counting system was sent to a computer for analysis.

CHAPTER 5

RESULTS

The following chapter presents the results of the fiber-optic coupled receiver system. The spectral characteristics and the total throughput efficiency of the receiver system are shown. Actual lidar signal returns measured with the receiver are compared to predicted signals. Signal-to-noise ratios for both online and offline lidar return signals are derived. Finally, an ozone DIAL measurement is presented with detailed error analysis and discussion on the limit of measurement range.

5.1 SPECTRAL CHARACTERISTICS OF FIBER-OPTIC COUPLED RECEIVER

The spectral characteristics of each component in the receiver were measured using the experimental setup in Chapter 4.1. The combined reflectance or transmittance of all the components yields the total throughput efficiency of the receiver. The amount reflected/transmitted light at 301 nm through the entire path of the receiver telescope is summarized in Figure 5.1. This figure shows that the total measured transmission of the receiver at 301 nm to the photocathode of the PMT is 37.2%, which is only 1.2% less than calculated in Chapter 3. The results are same for 311 nm except at the filter, which has a transmission of 40% at this wavelength resulting in a measured total throughput efficiency of 29.7%. This figure also shows that most of the transmission loss is due to the interference filter. It is evident that better filter technology at short UV wavelengths is needed to design higher efficient receiver telescopes in the future.

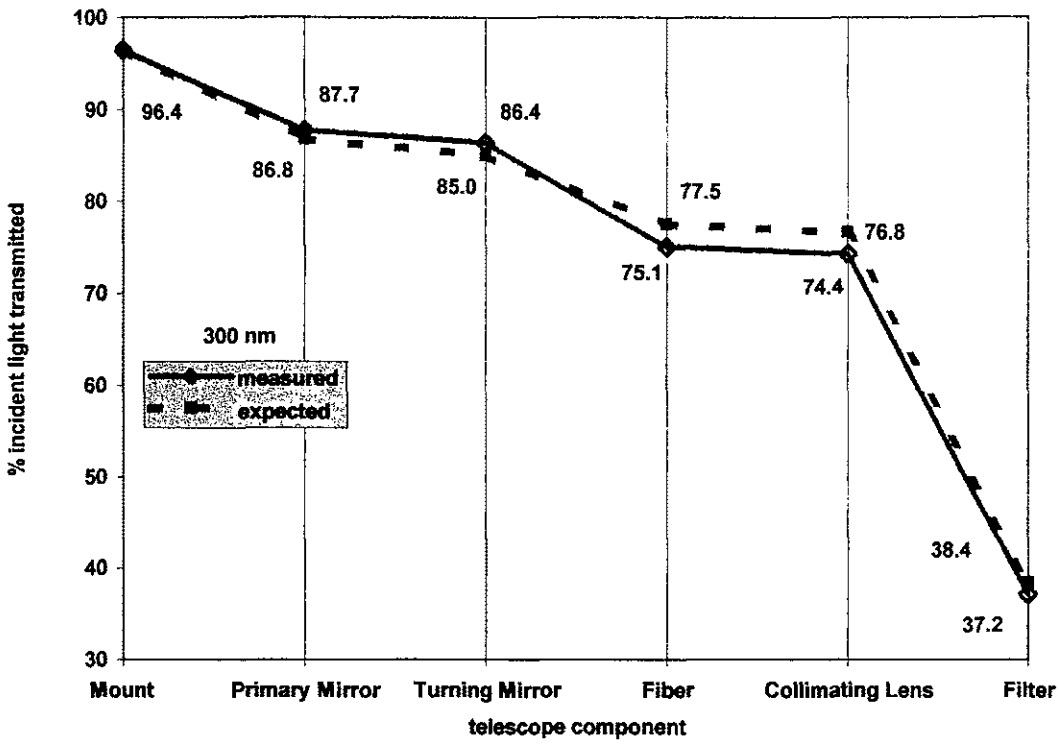

Figure 5.1 Transmission of incident light through entire path of the telescope receiver to the photocathode of the PMT detector

5.2 LIDAR SIGNAL RETURN MEASUREMENT

The backscattered lidar returns measured by a receiver system depend on atmospheric and instrument parameters. The amount of backscattered radiation and the total extinction of the signal are the unknown atmospheric parameters. The instrument parameters include the geometric setup and the total transmission of the telescope receiver. At UV wavelengths, most backscatter is from Rayleigh scattering by the air molecules present in the atmosphere. The total extinction depends upon the amount of aerosols and other species present that can cause other scattering effects and absorption.

5.2.1 *Lidar Return Signal Prediction*

Predicted lidar signals for this research were made using the photon counting form of the lidar equation (Eq. 2.19). The geometry of the system was modeled as a *biaxial* system with full overlap of the laser beam and telescope FOV at 5 km. The actual measured laser energy and total throughput efficiency of the receiver were used in the lidar equation. Tabulated results of Rayleigh scattering effects and signal attenuation at 300 nm were used to model the backscatter and total extinction coefficients [17] (see Fig 5.2). These tables are based on a standard atmosphere that assumes a low aerosol density in the upper atmosphere and no clouds.

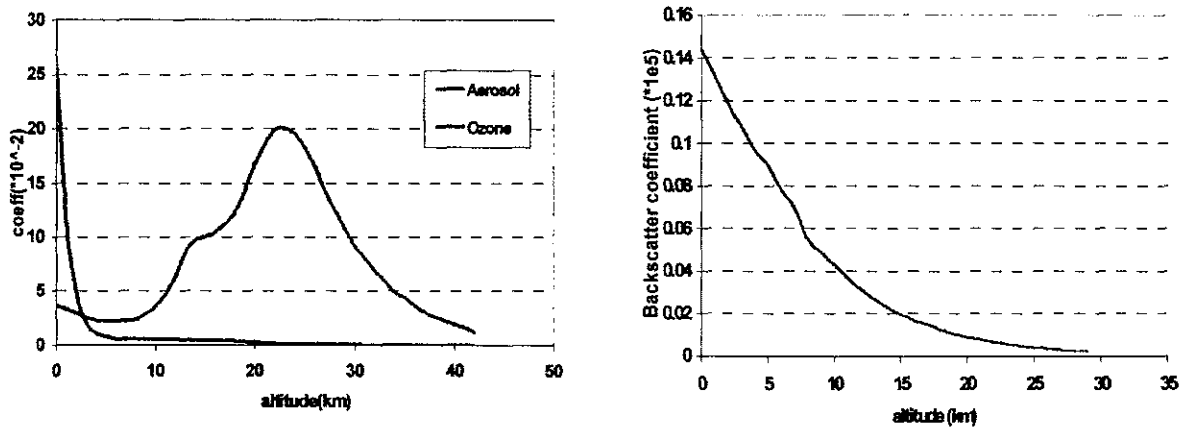

Figure 5.2 a) Extinction coefficients for aerosols and ozone. b) Rayleigh backscatter coefficients [17].

Although we cannot expect an exact signal prediction, these calculations give us an estimate of the expected performance of the lidar receiver. The predicted online lidar signal return at 300 nm for the fiber-optic coupled receiver is compared to an actual measurement of 301 nm made on June 18, 1998 (see Fig. 5.3).

As we can see in Figure 5.3, the predicted lidar signal return serves as a good model for calculating return signals expected for the fiber-optic coupled receiver system. The actual measured count rate is only different to about a factor of 2. The difference in the count rates for the predicted and actual return signal can be attributed to the estimations of the atmospheric parameters, especially to the fact that a standard ozone profile is assumed to exist.

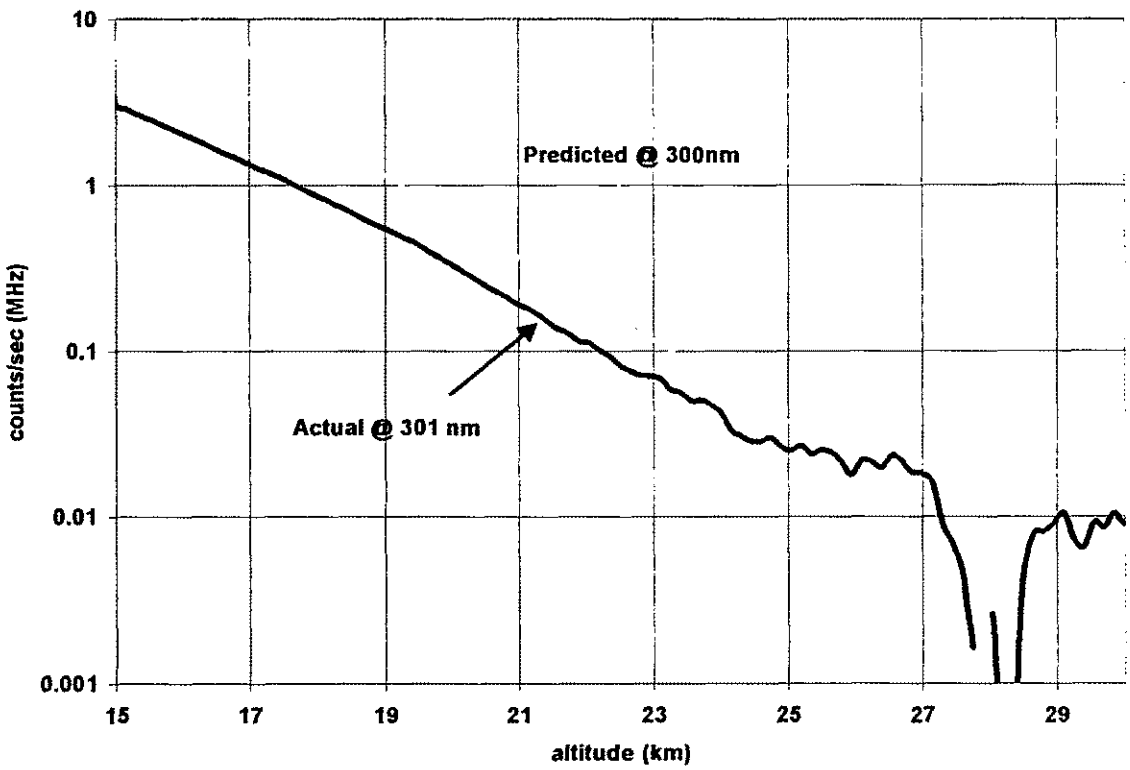

Figure 5.3 Predicted and actual online lidar return signals compared.

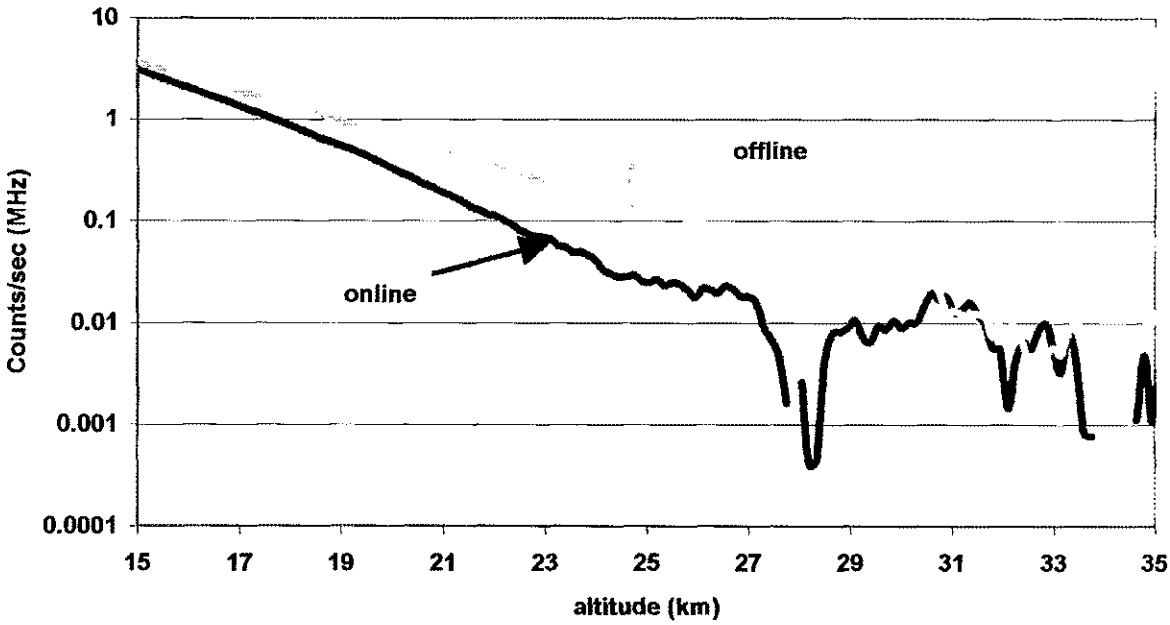

Figure 5.4 Online and Offline lidar return signals measured with fiber-optic coupled receiver system using photon counting

The background-subtracted lidar returns measured with the fiber-optic coupled receiver system are shown in Figure 5.4. The count rates for the online and offline signals at the gate turn on time were about 2.9 and 3.5 MHz respectively. Each lidar signal exhibits an exponential decay with altitude. As expected, the online return signal is attenuated by ozone absorption much more rapidly than the offline.

5.2.3 *Signal-to-Noise Ratio*

The background-subtracted lidar return signals were also entered into the signal-to-ratio (SNR) equation (Eq. 2.15)(see Fig. 5.5). The minimum detectable signal is usually defined where the SNR falls to unity [9]. The faster decaying online SNR falls to unity at about 27.5 km but the offline continues to about 32.5 km. The ideal situation would be that reliable DIAL measurements could be made to the limit of the online

signal, in this case 27.5 km. But in reality this is not the case; the noise in both signals has an effect and these errors propagate through the DIAL equation putting a more stringent SNR limit as will be seen in the next section.

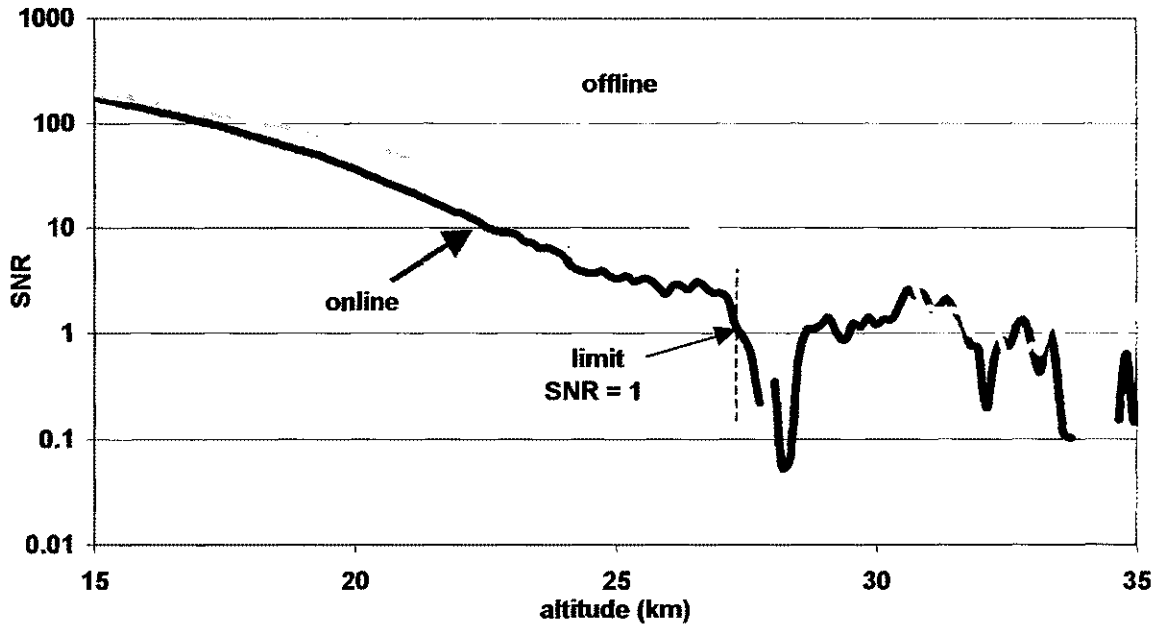

Figure 5.5 Signal-to-noise ratios of the online and offline lidar returns measured with the fiber-optic coupled receiver system.

5.3 STRATOSPHERIC OZONE DIAL MEASUREMENTS

The DIAL measurement in Figure 5.6 was taken at 9:00 p.m. on June 18, 1998. The Wallops Island ozone radio sonde data was taken at around 5:30 p.m. on June 18, 1998. The Wallops Island data is used only as a reference because the island is approximately 80 miles away from the NASA Langley Research Center. To decrease the natural fluctuations (standard deviation) that exist in the lidar return signals, we smooth the counts over a certain range. This helps to smooth out noisy DIAL calculations that result from raw data being plugged into the DIAL equation. In order to maintain consistency, we only smooth the counts over one range cell ΔR.

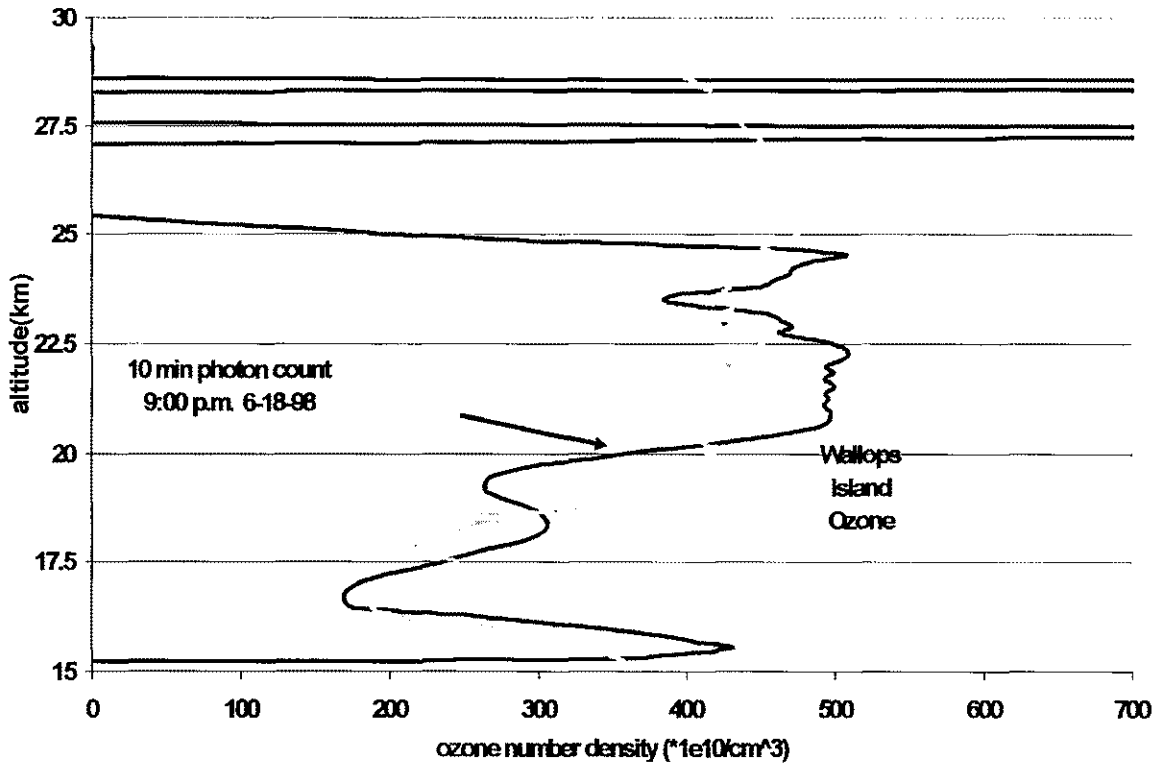

Figure 5.6 DIAL measurement of stratospheric ozone made on June 18, 1998.

The ozone number density was determined by entering the smoothed lidar signals measured by the photon counting system into the DIAL equation (Eq. 2.7). The difference in absorption cross-section between 301 nm and 311 nm is 2.1×10^{-19} cm^2 and the range cell used was 1050 meters.

Both the photon counting and the Wallops data show a high ozone number density feature at around 16 km. This feature is called a stratospheric intrusion where upper stratospheric air is transported down to where the stratosphere and troposphere meet [24]. This figure also shows that the number density of ozone increases with the altitude in the lower stratosphere and peaks at around 25 km. The DIAL measurement

made with the fiber-optic receiver then falls unrealistically to zero and begins to fluctuate after this altitude. This corresponds to where there is no more measurable signal to be detected. The fluctuations are a result of the DIAL calculation on the noise in the system.

Although the Wallops data serves as general reference to the validity of the DIAL measurement, further analysis can be done to determine the measurement range of the system. We can determine the measurement range by analyzing the relative error in the number density. The lidar return signals were entered into the relative density error equation (Eq. 2.9). Recall that the error in the DIAL measurement increases with altitude. If we define an acceptable systematic error of 10% from the DIAL measurement, then we can find the corresponding altitude at which this error occurs as shown in Figure 5.7.

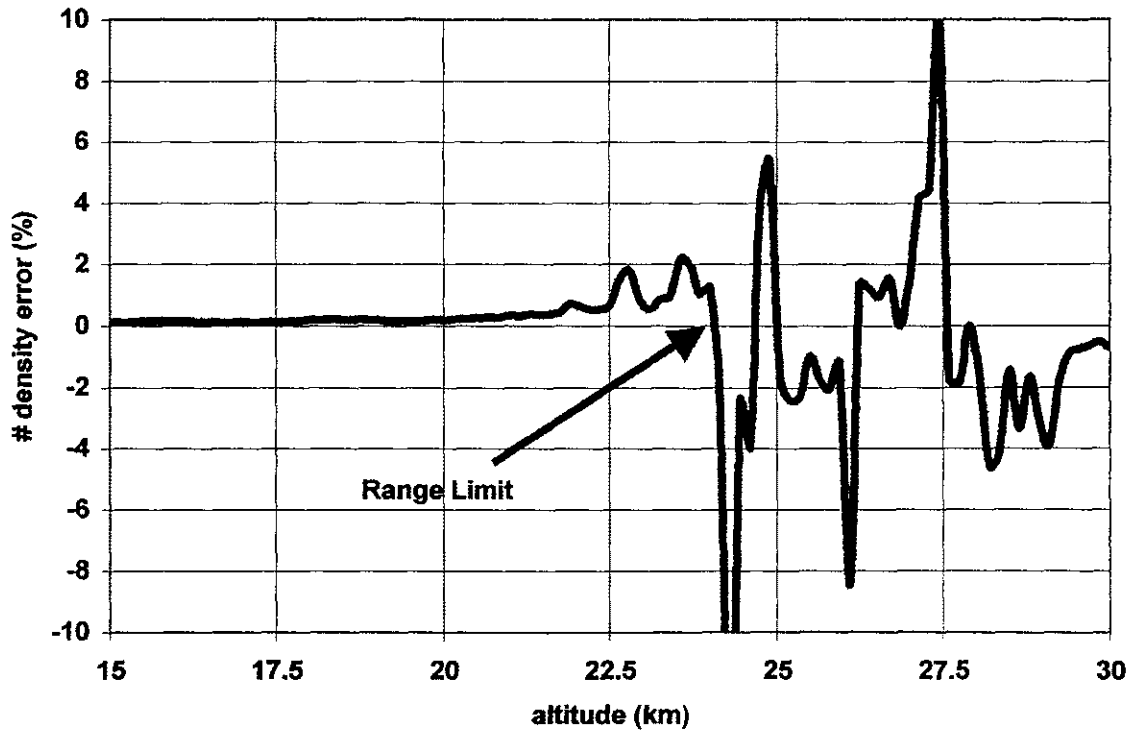

Figure 5.7 Error in DIAL calculation as a function of altitude.

This figure shows that the relative error in number density for this DIAL measurement is less than 2% up to an altitude of 24 km. The error dramatically increases to more than 10% after this altitude and begins to fluctuate rapidly. Recall that the SNR of the online signal fell to unity at 27.5 km for the lidar return measurement shown in Figure 5.5, but as shown by the relative error calculation, the DIAL measurement for this is limited to 24 km. Also, the DIAL calculation in Figure 5.6 decreases unrealistically to zero at 24.5 km. The corresponding SNR in the online signal at 24 km shown in Figure 5.5 is approximately 4.3. Therefore, DIAL measurements with less than 10% error can be made with this system under similar atmospheric conditions to 24 km or more realistically, to where the online SNR falls to approximately 4.3.

To extend the measurement range of the receiver system, it is necessary to increase the SNR as high as possible. As shown in Chapter 2.3.4, higher values of the SNR can be obtained by extending the photon counting time.

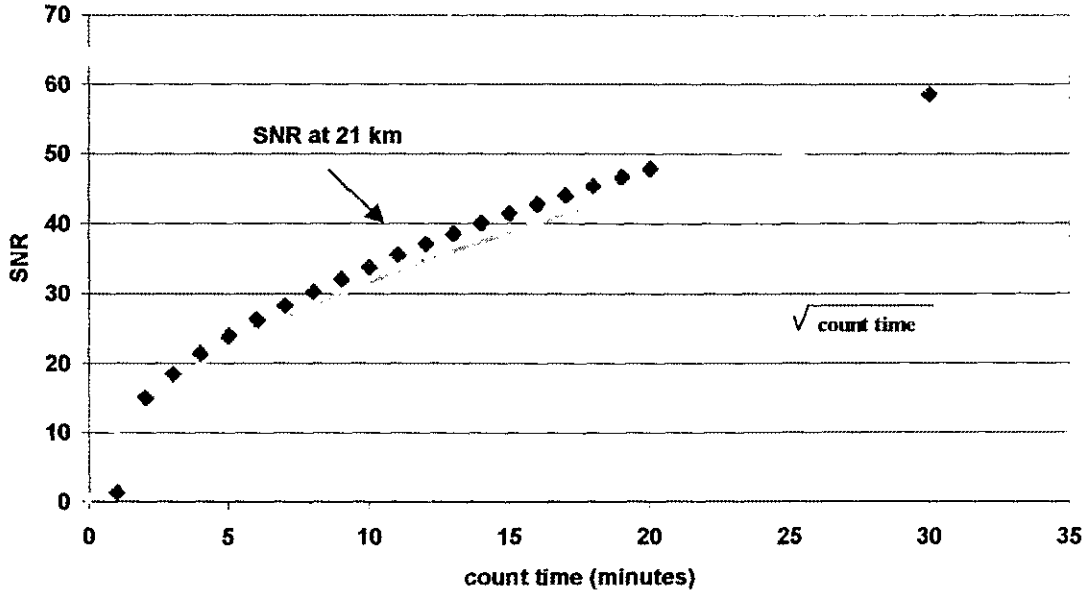

Figure 5.8 SNR at 21 km as a function of time.

Another DIAL measurement was performed on June 25, 1998 with a longer photon counting time. However, technical problems with the offline laser occurred so no DIAL measurement of ozone could be obtained. But, the increasing SNR effect can be seen by looking at just one signal. Figure 5.8 shows the effect of extending the count time up to thirty minutes to measure the online lidar return. The SNR at 21 km as a function of count time is shown. The SNR at one minute is relatively low and increases drastically by counting up to 10 minutes. As the count time continues up to 20 and then 30 minutes, the SNR in the signal increases less rapidly. In fact it increases with the square root of the count time. This is exactly what was predicted by Equation 2.15. Therefore, longer-range DIAL measurements of ozone should be possible by increasing the photon counting time.

CHAPTER 6

SUMMARY AND CONCLUSIONS

6.1 FIBER-OPTIC COUPLED RECEIVER SYSTEM

The fiber-optic coupled receiver system has a high overall throughput efficiency of 37.2% and 29.7% at the laser wavelengths of 301 and 311 nm. The complete receiver system contains few optical components, therefore limiting the amount of light loss by reflections. The carbon-epoxy tube provides a strong and lightweight housing that doesn't expand and contract under typical temperature environment changes. The fiber-optic cable provides a good means of guiding the collected light to the PMT detector with little transmission loss. The receiver FOV is 1.3 mrad, which is approximately two times larger than the divergence of the laser beams. Hence all the backscattered laser energy should is collected where the telescope FOV and laser beam fully overlap in the atmosphere. The receiver system is used in a *biaxial* arrangement to avoid near-field saturation of the PMT detector.

6.2 LIDAR RETURN SIGNALS

The photon counting form of the lidar equation serves as a good model for predicting lidar signals with the fiber-optic coupled receiver system. The actual measured count rates from a 301 nm lidar return were within a factor of two compared to the predicted return count rate. The difference in count rates can be attributed to the estimation of total extinction parameters especially the estimated number of ozone molecules that absorb the laser energy.

Lidar returns were measured for both online and offline wavelengths into the stratosphere. The PMT gating circuit was turned on at 15 km and count rates as high as ~4 MHz were measured at this altitude. The online and offline signals observed exhibited exponential decays with altitude. As expected, the online signal was more rapidly attenuated than the offline, especially where high ozone concentrations existed.

The signal-to-noise ratios of the online and offline lidar return signals were as high as 200 at the turn on altitude and fell to unity at 27.5 and 32.5 km respectively. These signal-to-noise ratios yielded a 12.5 km measurement range (15 - 27.5 km) of backscattered lidar returns in the stratosphere. This measurement range is mostly limited by the energies of the online and offline lasers. Further measurement ranges can be obtained by increasing the amount of laser energy transmitted into the atmosphere.

6.3 DIAL MEASUREMENT OF OZONE

The fiber-optic receiver system detected the online lidar signal as high as 27.5 km, but the DIAL measurement of ozone was limited to 24 km. This is due to the increasing error in the DIAL equation that occurs as altitude increases. The error in the DIAL calculation was less than 2% up to 24 km and dramatically increased to over 10% above this range. Comparison of the online SNR and the error in the DIAL equation yield valid ozone measurements where the online SNR is greater than 4.3.

The measurement of ozone with the fiber-optic coupled receiver system can be extended to higher altitudes by increasing the SNR in the return signals. Extending the photon counting time to 30 minutes increased the SNR. The SNR increased as the square root of time as predicted by theory presented in Chapter 2.

BIBLIOGRAPHY

1. M.H. Proffitt and A.O. Langford, "Profiling of Ozone in the Free Troposhere by the Lidar technique," Rev. Laser Eng. **23**, 104-107 (1995).

2. J.S.Wager, "Double Exposure," Nucleus **17**, 1-3 (1995).

3. J. Flaud, C. Camey-Peyret, C.P. Rinsland, M.A.H. Smith, V.M. Devi, *Atlas of Ozone Spectral Parameters from Microwave to Medium Infrared*, Academic Press Inc., New York, 1990.

4. E.V.Browell, "Differential Absorption Lidar Sensing of Ozone," Proceedings of the IEEE, **77**, 419-432 (1989).

5. V.E. Zuev, *Laser Beams in the Atmosphere*, Consultants Bureau, New York, 1982.

6. R.M Measures, *Laser Remote Sensing: Fundamentals and Applications*, Wiley, New York, 1984.

7. D.A. Richter, E.V. Browell, C.F. Butler, N.S. Highdon "Advanced airborne UV DIAL system for stratospheric and tropospheric ozone and aerosol measurements," *Advances in Atmospheric Remote Sensing with Lidar*, A. Amsnmann, R.Neuber, P.Rairoux, U.Wandinger(Eds.), 395-398, 1996.

8. G. Asrar, *Theory and Application of Optical Remote Sensing*, Wiley, New York, 1989.

9. *Photon Counting using Photomultiplier Tubes* , (Hammamatsu Technincal Information, Sept. 1996).

10. E. Hergert & C. Walling, "Photomultiplier Tubes See the Light," Photonics Spectra, 98-102, (Dec. 1996).

11. E.Hergert, "Photomultiplier Tubes count photons," Laser Focus World, 129-134 (Nov. 1997).

12. I. Iikura, N. Sugimoto, Y. Sasano, and H. Shimzu, "Improvement on lidar data processing for stratospheric aerosol measurements," Applied Optics, **26**, 5299-5306(1987).

13. H. S. Lee, G.K. Schwemmer, C. L. Korb, M. Dombrowski, and C. Prasad, "Gated photomultiplier response characterization for DIAL measurements," Applied Optics, **29**, 3303-3315(1990).

14. I. S. McDermid, S. M. Godin, and L. O. Lidqvist, "Ground-based laser DIAL system for long-term measurements of stratospheric ozone," Applied Optics, **29**, 3603-3612 (1990).

15. I. S. McDermid, T. D. Walsh, A. Deslis, and M. L. White, "Optical systems design for a stratospheric lidar system," Applied Optics, **34**, 6201-6210(1995).

16. R.E.W. Pettifer, "Signal-Induced noise in lidar experiments," J. Atmospheric and Terrestrial Physics, **37**, 669-673(1975).

17. L. Elterman, "UV, Visible, and IR Attenuation for Altitudes to 50 km, 1968", Environmental Research Paper No. 285, Air Force Cambridge Research Laboratories, Bedford, MA, April 1968.

18. B. Hunt, Lidar Technical Notes, **9**, Wyle Laboratories, 1996.

19. *Laser Radar Systems and Applications,* (University of Central Florida, Orlando, 1991).

20. J.Wilson & J.F.B. Hawkes, *OptoElectronics,* 2nd Ed., Prentice Hall, 1989.

21. L.C. Shen & J.A. Kong, *Applied Electromagnetism,* Prindle, Weber, & Schmidt, Boston, 1987.

22. J.A. Buck, *Fundamentals of Optical Fibers,* Wiley, 1995.

23. B.A. Eccles, "Development of a Photon Counting System for Ozone Differential Absorption Lidar Signal Detection," Old Dominion University, 1997.

24. C.F. Butler, E.V. Browell, M.A. Fenn, W. Grant, M. Clayton, "Ozone and aerosol distributions in the Pacific as observed by NASA's airborne UV DIAL system," Proceedings of SPIE, *Optical Remote Sensing for Industry and Environmental Monitoring*, 3504, 174-181 (1998).

APPENDIX A

NASA/TM-1998-207674

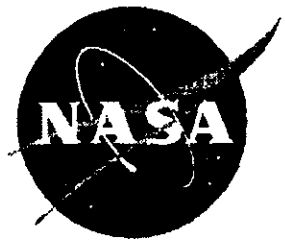

Signal-Induced Noise Effects in a Photon Counting System For Stratospheric Ozone Measurement

David B. Harper
Old Dominion University, Norfolk, Virginia

Russell J. DeYoung
Langley Research Center, Hampton, Virginia

APPENDIX A

SIGNAL-INDUCED NOISE EFFECTS IN A PHOTON COUNTING SYSTEM FOR STRATOSPHERIC OZONE MEASUREMENT

INTRODUCTION

One very sensitive method of optical signal detection is called photon counting. Light falls on the photosensitive cathode of a photomultiplier tube (PMT) creating electrons that are multiplied through a dynode chain resulting in an output pulse at the anode. Ideally, each photon received produces an electrical pulse at the anode of the PMT that is then sent through an amplifier and into a pulse discriminator. The discriminator has a set output pulse width and threshold setting. The threshold is set just above the noise level in the system; therefore only pulses above this level are counted. Each pulse sent by the discriminator has an equal pulse width and height set by the discriminator. These pulses are sent to a multi-channel scaler and averaging memory that counts the number of pulses received from the discriminator and stores them into typically one microsecond bins (see fig 1). The main advantages of photon counting are: 1) more sensitive detection of very low light levels that do not produce analog signals and 2) elimination of electronic baseline effects. If the noise and light signal are properly distinguished, low light levels (single photon counts) can be detected.

In a typical DIAL (Differential Absorption Lidar) system, two laser pulses, separated in time, are emitted by the laser system. These pulses, one tuned to high ozone absorption (on-line) and the other tuned to a lower absorption (off-line), are backscattered by the atmosphere creating a return light signal. This signal is received by a telescope, passed through a narrow band filter, and focused onto a photomultiplier detector. When ozone is present in the atmosphere, the on-line signal decay is faster than that of the off-

line due to the absorption by ozone. The difference in the on-line and off-line decay rates of the returned signal yields the number density n of ozone as a function of altitude as seen in Equation (1)

$$n = \frac{1}{2 \cdot \Delta\sigma \cdot \Delta R} \cdot \ln\left(\frac{P_{off}(R_2) \cdot P_{on}(R_1)}{P_{off}(R_1) \cdot P_{on}(R_2)}\right) \tag{1}$$

where $\Delta\sigma$ is the difference of on-line and off-line cross-sections, $\Delta R = (R_2 - R_1)$ is the range cell, and P(R) are the powers of the on-line and off-line signals at altitude R.[1]

It is usually assumed that the signal output of a PMT is linearly proportional to the input light intensity and when no light is present there is only a small DC electrical output known as dark current. While this is a good assumption for low light levels, the PMT output is nonlinear for high input light intensities. Also, when the PMT is exposed to momentary high light intensities, the output does not return to the dark current level immediately but instead decays slowly. The latter effect is called signal-induced noise (SIN), which can limit the range and accuracy of ozone measurements in a DIAL system unless it is compensated for in the data analysis.

Grant *et.al* have noted that the airborne UV DIAL data are systematically lower than those of other instruments at higher altitudes. This discrepancy could be caused by signal-induced noise, which would tend to measure less ozone.

In this technical memorandum we will describe the effects of signal-induced noise on a stratospheric ozone photon counting system. The nature of SIN will be evaluated with respect to PMT type, voltage, incident wavelength, and incident intensity. These

results have provided for a greater understanding of this problem, and this should lead to an approach for eventually neutralizing this effect.

THE EFFECT OF SIGNAL-INDUCED NOISE

SIN is a common effect resulting when a PMT is saturated, for a brief moment, with a high intensity light pulse. The effect is shown schematically in Figure 2. After the laser pulse is sent into the atmosphere a very large light return, from either the near field atmosphere or a cloud, causes the PMT to momentarily saturate. The PMT is gated off at this time so no signal is seen at the anode. When the PMT gate is turned on, the far field light return from the atmosphere is observed. This signal is distorted because of the addition of SIN to the received light signal causing a slower than expected decay of the atmospheric signal return. The true signal return and SIN cannot be separated because they are both derived from the same laser pulse. The large number of electrons emitted from the photocathode during saturation appear to charge up some internal components, which then emits electrons very slowly resulting in a long decay SIN signal. The temporal characteristics of SIN typically follow that of decaying exponentials.[3,4,5,6] If SIN is present, its decaying exponential baseline is added to the real lidar return signal resulting in a longer signal decay than expected. This effect can cause large errors in DIAL measurements, particularly in the far field. For example, unless measured without a lidar return present, the unknown baseline cannot be subtracted from returned light signals. This can lead to unrealistic negative ozone measurements because the decay rate of the on-line signal may be slower than the decay rate of the off-line signal. Also, when the lidar is pointed in the zenith, the returned atmospheric light signal from high altitudes

is extremely low. When the returned light level is low enough, the signal cannot be distinguished from the SIN therefore limiting the overall measurement range of the lidar system. Electrical gating of the PMT has been shown to reduce SIN but not eliminate it.[4]

Since electrical gating of the PMT does not eliminate SIN, other methods of reduction and/or removal of the effect are necessary. Mechanically shielding the PMT with a chopper fan while it is gated off, would seem to be the most effective way of eliminating SIN. The chopper needs to close for a few tens of microseconds to protect the PMT from the near field return from the on-line laser, open for typically 270usec(~40km) to allow the lidar return from the on-line laser pulse to be detected, and repeat this process for the off-line laser pulse. This fast timing requires a very fast and stable chopper, which is difficult to implement because most choppers have a low stability. Another method would be to model the SIN response and try subtracting this from the lidar returns mathematically.[3,4,5,6] This method has been shown to improve DIAL measurements but increases the complexity of the data analysis.

One way to see the effect of SIN is to range-correct the lidar return light signal and compare it to the standard molecular density profile of the atmosphere. The light backscattered from each cubic centimeter of atmosphere at a given altitude should directly follow the atmospheric density. Range-correction of a returned signal is done by mathematically compensating for the $1/R^2$ geometric decrease in collected backscattered signal with range and correcting for the atmospheric attenuation between the lidar and scattering range. The atmospheric attenuation results from aerosol scattering, Rayleigh scattering, and absorption at a given wavelength, which can be summed into a total extinction coefficient over a given optical depth. These total extinction coefficients have

been estimated at many wavelengths by Elterman[7]. The total range-corrected signal is then given by Equation (2)

$$S(R)_A = \frac{P(R)_A \cdot R^2}{\exp(-2 \cdot OD)} \tag{2}$$

where $P(R)_A$ is the power of the received signal from altitude R, OD is the optical depth[7], $S(R)_A$ is the atmospheric backscattering coefficient (which at high altitudes is primarily molecular scattering), and C is a system constant.

Ideally, the corrected $S(R)_A$ signal should follow the decaying molecular density profile as a function of increasing altitude. If SIN is present or if the background is not properly subtracted from the return light signal then the range-corrected signal will not follow the molecular density. Instead, at higher altitudes where the return signal is low, the SIN will cause the range-corrected signal to grow as shown in Figure 3.

The photon counting data in Figure 3 resulted from a twenty-minute measurement period performed at night. The measured background was negligible. The laser wavelength was 300 nm and the receiver telescope was a 14 inch Cassegrian type. The laser beam was emitted from the system to the atmosphere along the outer edge of the lidar telescope. This configuration caused a large near field return to be seen by the telescope enhancing the SIN effect. In this figure, the lidar return follows the molecular density to a range of 19.5 km where SIN dominates over the lidar return causing the signal to depart from the atmospheric density. Below 19.5 km, the signal-to-noise ratio is high and the lidar return follows the molecular density. Above 19.5 km, the signal-to-

noise ratio is low due to the fact that the actual lidar return signal follows the molecular density but the SIN does not. SIN was found to follow a much slower decay with time.

EXPERIMENTAL SETUP

In order to understand the basic characteristic of SIN, an experiment was devised to determine the effect of PMT tube type, voltage, incident light wavelength and incident light intensity on SIN. A pulsed light source would be used to saturate the PMT, and at some later time, the PMT gate would be turned on. The resulting SIN was measured with a two-minute accumulation period. In each case the pulse width and threshold of the discriminator were set at 5 ns and 30 mV respectively.

Two different light sources were used to study the SIN-PMT response. The first light source for the experimental setup, shown in Figure 4, was a 1000 W-xenon lamp with an adjustable current power supply. A 57 mm condenser lens, placed in the lamp housing's optical axis, allowed beam-focusing adjustments. The light was directed into a high intensity grating monochrometer that was adjustable from 180 to 800 nm. Adjustable slits on the input and output sides of the monochrometer allowed control of light intensity. The complete light source was attached to a "light" box that blocks out all unwanted light. The second experimental setup used a blue LED with a center wavelength at 470 nm as shown in Figure 5.

The light from either the LED or the Xe lamp was passed through a small aperture that was placed close to a chopper fan. The aperture hole and the two chopper fan slits were each approximately 2 mm in width. By using a chopper, it could be assured that no light fell on the PMT when the PMT gate opened. Neutral density filters were used to vary intensities of the incoming light pulses. The fiber-optic cable that joined the two

light boxes was a 1mm diameter UV grade quartz fiber. The PMT was mounted in the second light box where the output of the fiber was placed near the PMT photocathode.

The entire photon counting system was triggered from a synchronization pulse coming from the chopper fan controller. The chopper fan rotated at 50 Hz providing a 100 Hz pulse rate from the two fan slits. The count rates were set to be 10, 1, and 0.1 times saturation by using corresponding neutral density filters. The saturation points for these tubes were experimentally determined by increasing the input light intensity while monitoring the PMT output. The saturation level was defined at the intensity level where the PMT output was no longer increasing linearly with the input light.

Signal-induced noise effects were studied for several PMT tubes with similar physical structures. All the tubes used were linear focused with a 12 dynode chain. The characteristics of each tube are summarized in Table 1.

PMT Manufacturer-Type-Serial #	Photo-Cathode Material	Quantum Efficiency @300nm (%)	Dynode Chain Material	PMT Voltage
EMI-9214Q-#5162	Bialkali Sb-K-Cs	25.2	CsSb	1200
EMI-9214Q-#5150	Bialkali Sb-K-Cs	31.5	CsSb	1200
EMI-9954Q-#5358	Bialkali Sb-Rb-Cs	26	BeCu	1800
EMI-9817Q-#3236	S20 Trialkali Na-K-Sb-Cs	23.2	BeCu	1850

Table 1. PMT tube characteristics

The 9214Q tubes are used in the ozone DIAL system because of their high quantum efficiency in the UV range and stable gain versus changing pulse rate. The 9954Q and

9817Q were used for a comparison because of their similar physical structures with different photocathode and dynode chain materials.

EXPERIMENTAL RESULTS

With saturating light pulses, we observed SIN responses that followed a combination of decaying exponentials over a 550 usec observation time. The SIN effect was observed at different wavelengths, different PMT voltages, and different count rates (intensities). SIN response was also compared for three different tube types. The results are summarized as follows:

A. Light Wavelength Effect on SIN

Figure 6 shows the first 50 usec of the SIN PMT response for tube 9214Q #5162 at input light wavelengths of 300, 350, and 400 nm. The input light intensity was kept constant at 10 times saturation level. For all wavelengths of light, the time constant of the SIN effect was 35 usec as shown by the straight line in Figure 6. This indicates that wavelength is not a major driver for SIN as long as the photocathode electron emission intensity is constant. SIN appears to be more a function of the number of electrons emitted from the photocathode. A higher quantum efficiency PMT would emit more electrons resulting in a greater SIN effect.

B. SIN and PMT Voltage

Figure 7 shows the SIN PMT response at different PMT dynode chain voltages for tube 9214Q #5162. Once again the intensity was kept constant for each voltage. The amplitude of the SIN did increase as PMT voltage increased which is expected

due to the higher gain of the PMT at higher dynode chain voltages. The time constant differed by only 2 usec for a PMT voltage range of 200 volts which indicates that only the amplitude of SIN is effected by changing PMT voltage and not the decay rate.

C. Input light Intensity and SIN

SIN response for the PMT 9214Q #5150 at three different 300 nm wavelength light intensities is shown in Figure 8. The light intensities were 0.1, 1, and 10 times saturation level of the PMT. The response shows that SIN is a combination of three different decaying exponentials with decay constants of 34 usec, 49 usec, and 525 usec. This suggests that there are three different mechanisms causing SIN for this PMT. The third component of the 0.1 saturation level can not be seen because it has already decayed into the dark count level of the PMT. The amplitude of the SIN increased linearly with increasing light intensity but the decay constants at each intensity remained the same. This shows that only the amplitude of SIN is effected by different light intensities but the temporal behavior remains unchanged.

D. Different PMT Types and SIN

SIN response for three different PMT tubes (9214Q# 5150, 9817Q #3236, and 9954Q #5358) with similar physical structures is shown in Figure 9. The light intensity was set to 10 times saturation for each tube. The decay constants for the initial fast component and the slowest third component are similar in each tube. This indicates that tubes with similar physical structures should exhibit similar SIN

responses. With a different PMT structure we would expect different SIN decay time constants.

CONCLUSIONS

Photon counting offers an extremely sensitive detection method for measuring stratospheric ozone with a DIAL system. However, the range of the system using this technique can be limited by signal-induced noise effects caused by high intensity near field or cloud returns.

In this technical memorandum, we have characterized SIN responses to varying parameters of the incident light on the PMT. These varied parameters included incident wavelength, PMT voltage, incident intensity, and tube type. We found that only the amplitude of the SIN was effected by varying PMT voltages and light intensities. The amplitude increased linearly as input light intensity increased. Different incident wavelengths at the same intensity did not effect the amplitude or the temporal behavior of the SIN response. Finally, different PMT tubes with similar physical structures exhibited similar SIN responses although with different amplitudes. The different amplitudes can be attributed to the different gains and operating voltages of each tube.

These results suggest that SIN is caused by photocathode electron dynamics such as charge accumulation on internal PMT surfaces. These surfaces then emit the electrons slowly resulting in a long decay noise signal. With the SIN responses characterized we can now try to develop a method to reduce or eliminate SIN in DIAL systems.

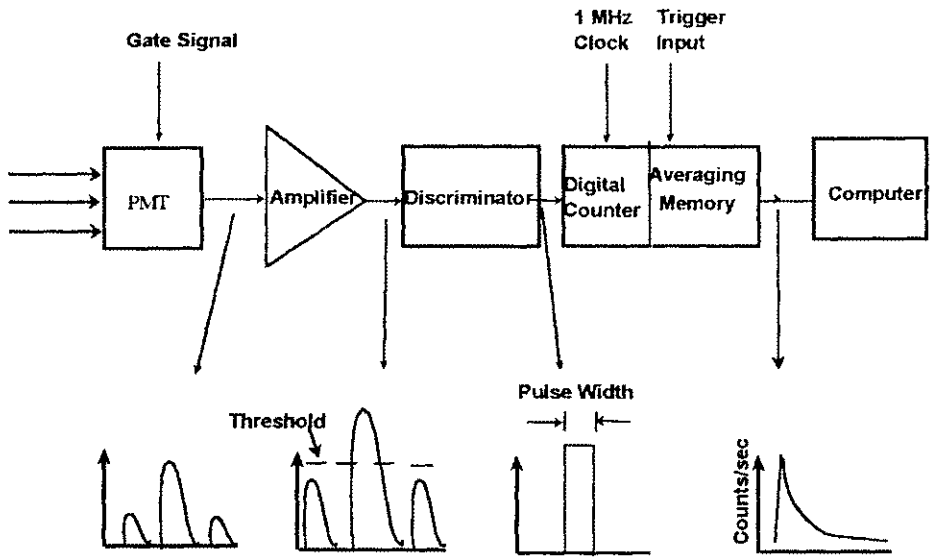

Fig 1. Block diagram of photon counting system.

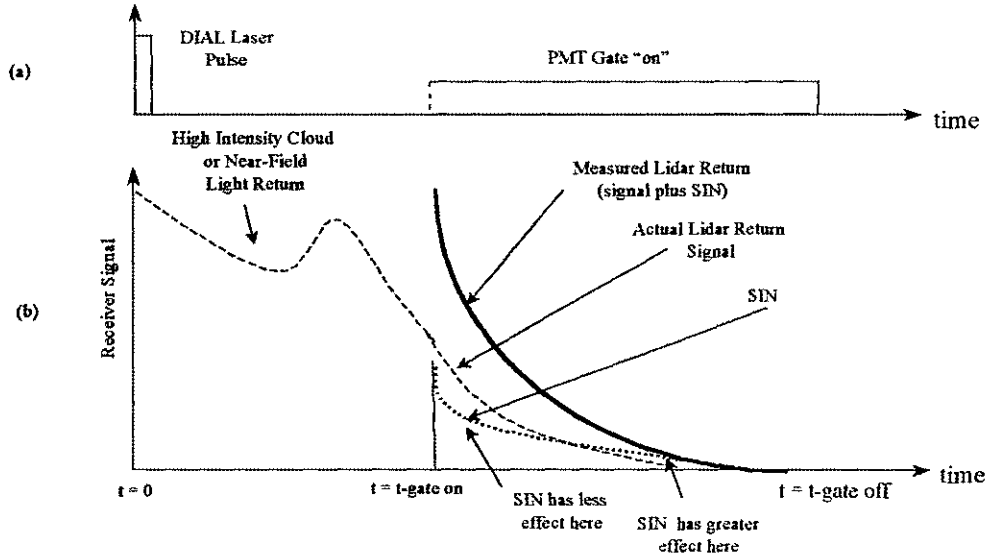

Fig 2. (a) Laser pulse and PMT Gate timing (b) Measured Lidar Return showing SIN effect caused by high intensity light falling on PMT while PMT is gated off

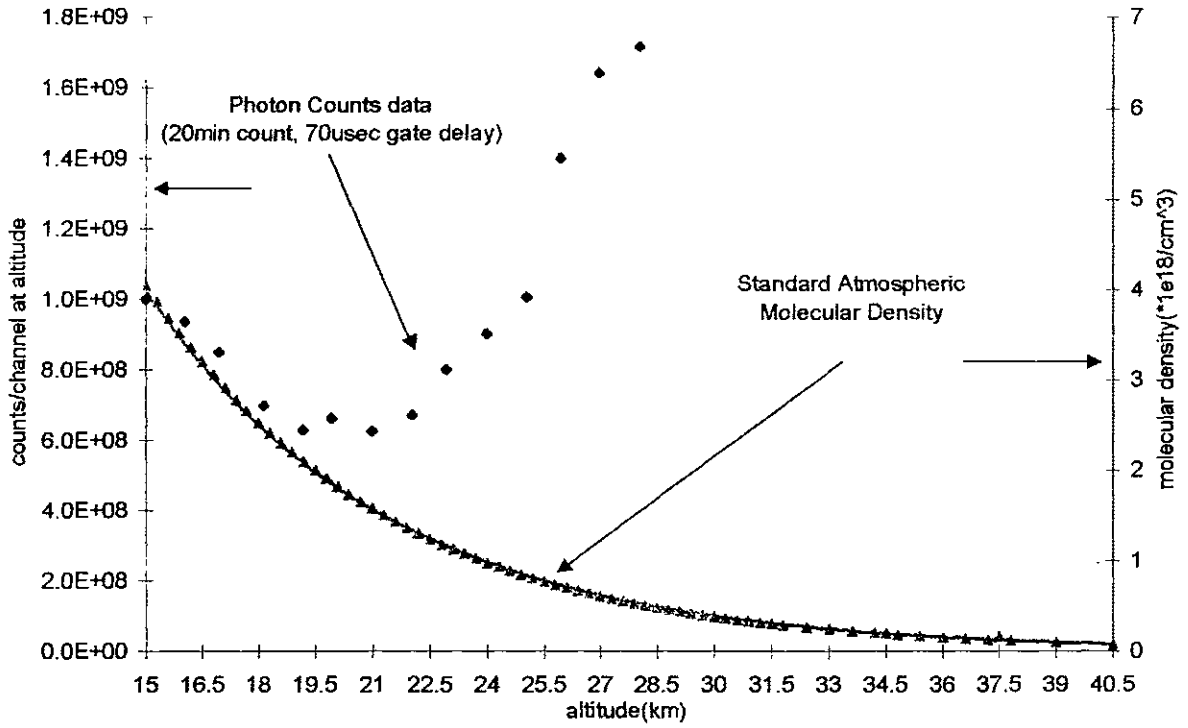

Fig 3. Range-corrected photon counts and atmospheric molecular density vs altitude.

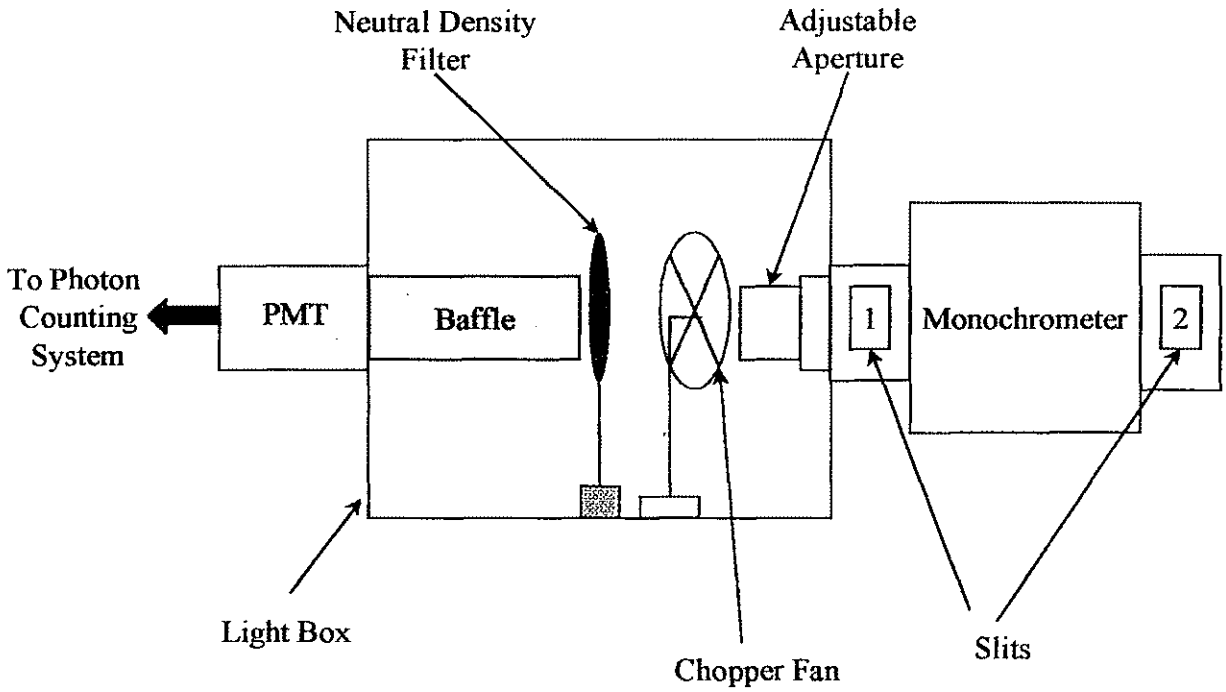

Fig. 4 Experimental Setup

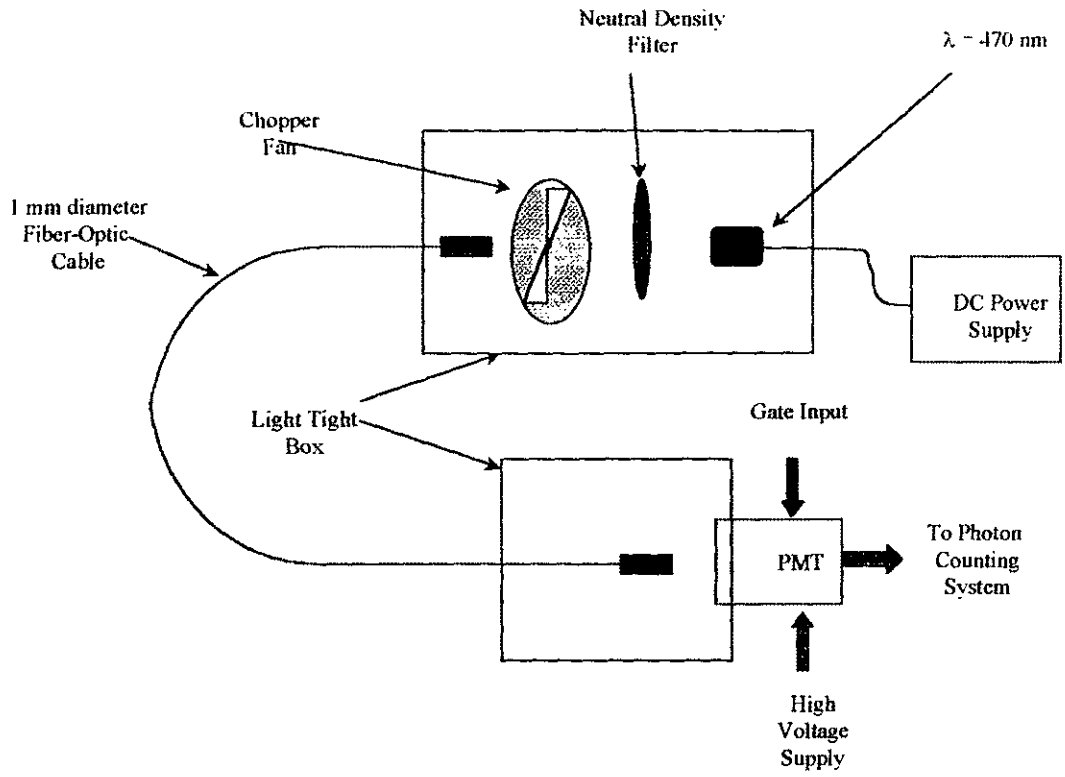

Fig. 5 Experimental setup for intensity SIN measurements.

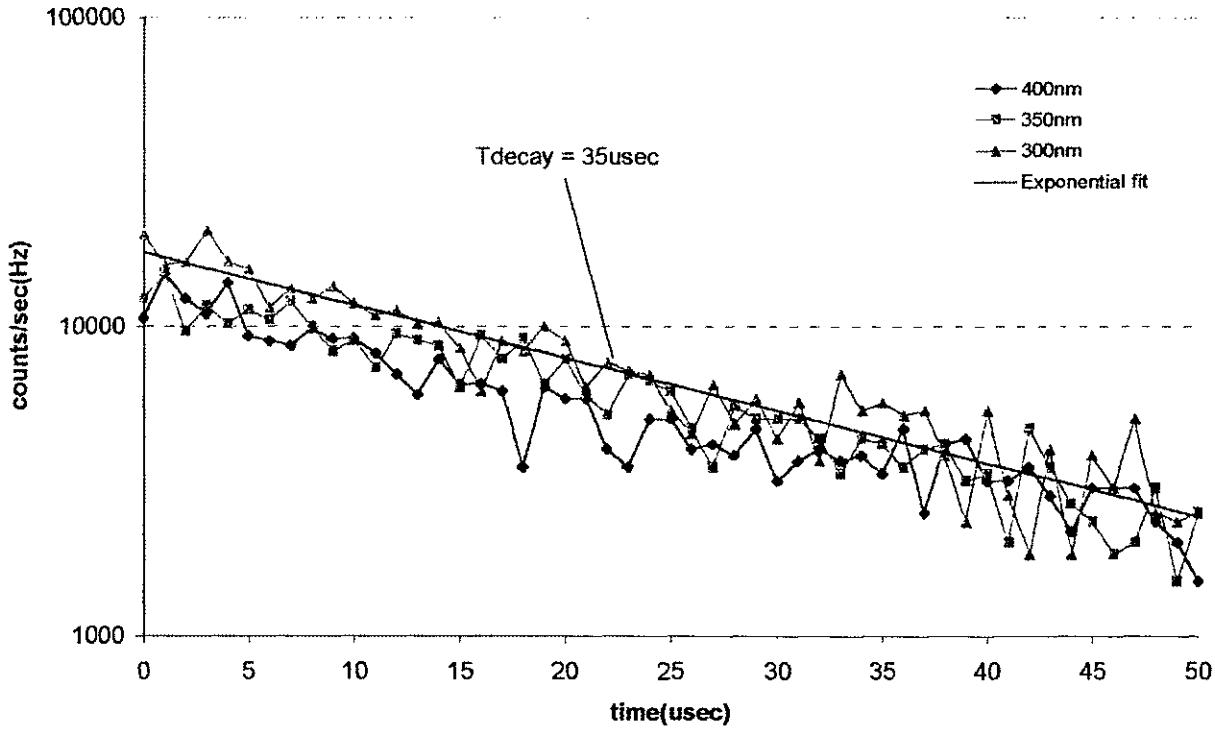

Fig 6. Signal-Induced noise at different wavelengths with same count rate(10*saturation) for PMT(EMI 9214 #5162).

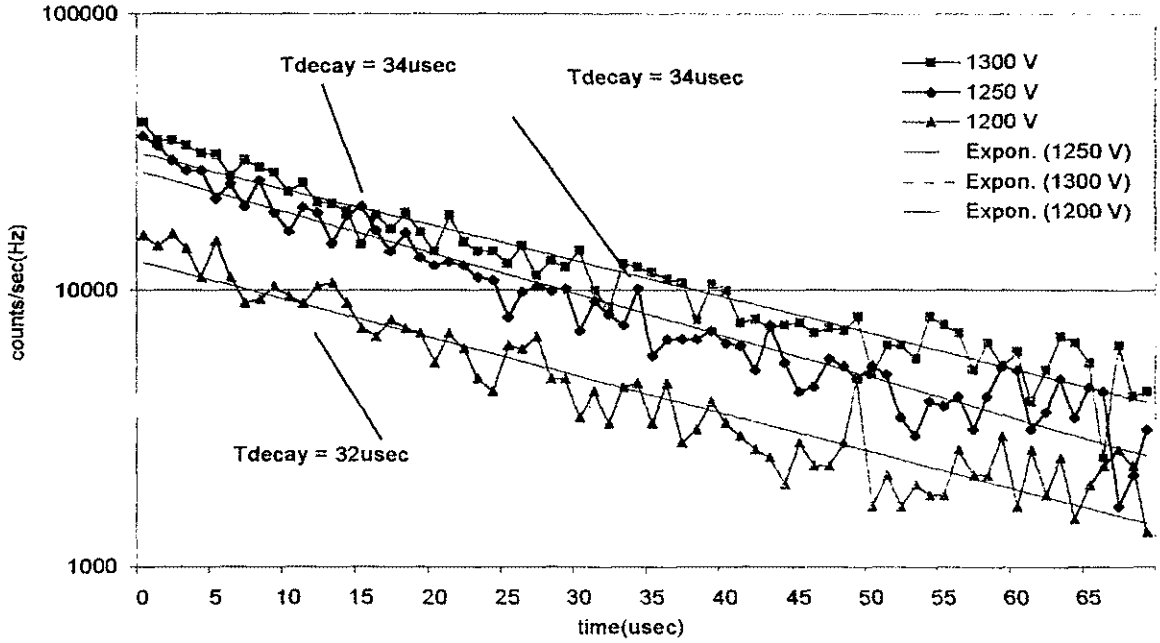

Fig 7. Signal-Induced noise for different PMT voltages using PMT(EMI 9214 #5162).

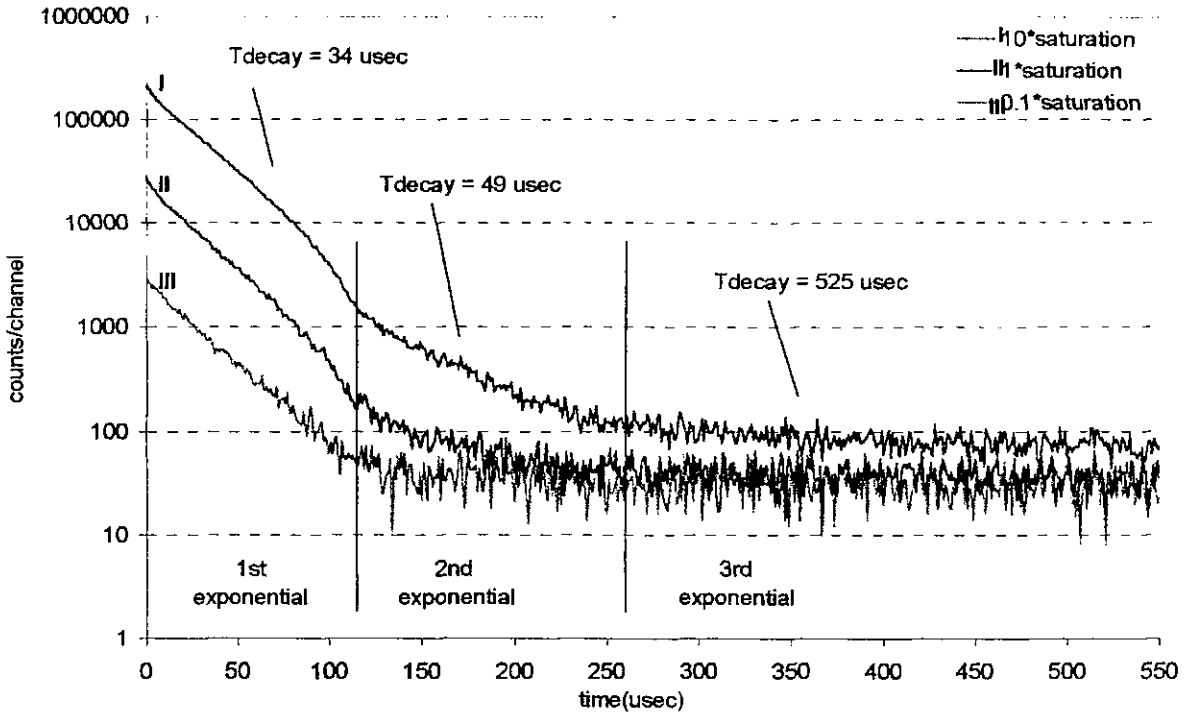

Fig 8. SIN response at different light intensitites(defined as factor times saturation level) for PMT tube 9214Q#5150.

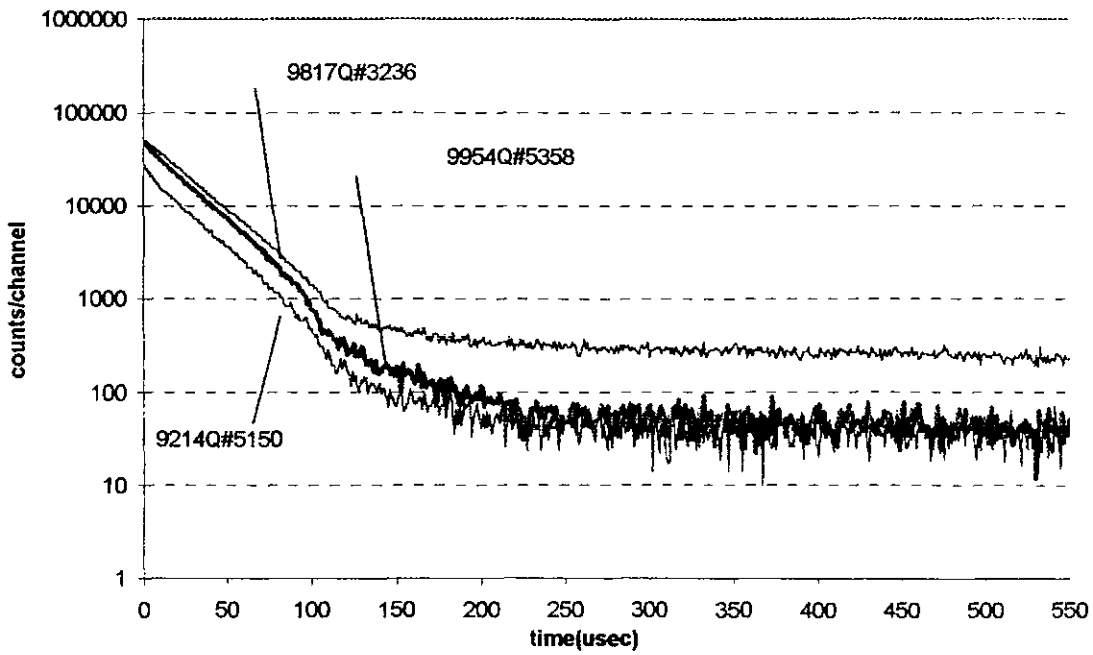

Fig 9. SIN response for three different PMTs.

APPENDIX B

PARTIAL PROGRAM LISTING

A partial listing of the code for this application follows. Only the essential classes are listed since there is a lot of overhead code associated with WINDOWS™ features. The photon counting program application was developed under Microsoft Visual C++™ to run under a WINDOWS 3.1™ or WINDOWS 95™ operating system. The main function of the program is to control the photon counting system and acquire data when a photon count is complete. The program also has additional data analysis features to perform real time DIAL calculations of ozone from the lidar returns retrieved form the photon counting system memory. This application also saves important user information that includes the laser and photon counting system setups.

```
// o3lidvw.cpp : implementation of the Co3lidarView class
//

#include "stdafx.h"
#include "o3lidar.h"
#include "windecl.h"
#include <stdio.h>
#include <stdlib.h>
#include <iostream.h>
#include <math.h>
#include <fstream.h>
#include "dialeqn.h"
#include <string.h>
#include <ctype.h>
#define  data_file "counts1.txt"

//////
// Co3lidarView
IMPLEMENT_DYNCREATE(Co3lidarView, CView)

BEGIN_MESSAGE_MAP(Co3lidarView, CView)
      //{{AFX_MSG_MAP(Co3lidarView)
      ON_COMMAND(ID_COUNT_SETTINGS, OnCountSettings)
      ON_COMMAND(ID_GRAPH_COLOR, OnGraphColor)
      ON_COMMAND(ID_GRAPH_LINE, OnGraphLine)
      ON_COMMAND(ID_GRAPH_ANISTROPIC, OnGraphAnistropic)
      ON_COMMAND(ID_GRAPH_ISOTROPIC, OnGraphIsotropic)
      ON_COMMAND(ID_COUNT_PHOTON_COUNT, OnCountPhotonCount)
      ON_COMMAND(ID_GRAPH_SCALING, OnGraphScaling)
      ON_WM_LBUTTONDBLCLK()
      ON_WM_RBUTTONDBLCLK()
      ON_COMMAND(ID_HELP_DAVID, OnHelpDavid)
      ON_COMMAND(ID_FILECONVERSION_CHANGETOTEXT,
OnFileconversionChangetotext)
      ON_COMMAND(ID_FILECONVERSION_OPENFILECOUNTSTXT,
OnFileconversionOpenfilecountstxt)
      ON_COMMAND(ID_FILECONVERSION_CLOSEFILE,
OnFileconversionClosefile)
      //}}AFX_MSG_MAP
      // Standard printing commands
      ON_COMMAND(ID_FILE_PRINT, CView::OnFilePrint)
      ON_COMMAND(ID_FILE_PRINT_PREVIEW, CView::OnFilePrintPreview)
END_MESSAGE_MAP()

////////////////////////////////////////////////////////////////////////
//////
// Co3lidarView construction/destruction

Co3lidarView::Co3lidarView()
{
   //initialize variables and set flags
      m_pGraph                    = NULL;
        bFirstDraw               = TRUE;
        m_bHighCount             = FALSE;
        GetGraph()->m_bHighData  = FALSE;
        m_bTemp                  = FALSE;
        m_Range                  = 300;
```

```
        m_iFileNumber            = 1;
}

CGraph* Co3lidarView::GetGraph()
{
      if(m_pGraph == NULL)
      {
            m_pGraph = new CGraph;
      }
      return m_pGraph;
}
////////////////////////////////////////////////////////////////////////////
//////
// Co3lidarView drawing
void Co3lidarView::OnDraw(CDC* pDC)
{
      Co3lidarDoc* pDoc = GetDocument();
      ASSERT_VALID(pDoc);
      int iLoop;//loop counter
    int iSize;//size of array

    //update view members with document members
    m_AmpType          = pDoc->m_AmpType;
      m_AmpGain          = pDoc->m_AmpGain;
      m_DiscName         = pDoc->m_DiscName;
      m_PMTType          = pDoc->m_PMTType;
    m_PMTSerialNumber = pDoc->m_PMTSerialNumber;
    m_GateDelay        = pDoc->m_GateDelay;
    m_PulseRate        = pDoc->m_PulseRate;
    m_TotalCounts      = pDoc->m_TotalCounts;

    iSize = pDoc->m_PhotonCounts.GetSize();
    if((iSize != 0)&& (bFirstDraw == TRUE))
      {
        m_PhotonCounts.RemoveAll();
         for (iLoop = 0; iLoop < iSize; iLoop++)
           {
             m_PhotonCounts.Add(pDoc->m_PhotonCounts.GetAt(iLoop));
           }
        FindMaxValue2(m_PhotonCounts);
        ////////////////////////////////////////////////////
        if(m_bHighCount)
          {
            if(m_bTemp)DivideDataby1000();
            GetGraph()->SetDataPoints(m_HighPhotonCounts);
          }
        else
          {
            GetGraph()->SetDataPoints(m_PhotonCounts);
          }

        bFirstDraw = FALSE;
      }
      else
        {
          bFirstDraw = FALSE;
        }
```

```
    CRect rc;
      GetClientRect(&rc);
      GetGraph()->Draw(pDC, rc);

}
////////////////////////////////////////////////////////////////////////////
//////
// Co3lidarView diagnostics

#ifdef _DEBUG
void Co3lidarView::AssertValid() const
{
      CView::AssertValid();
}

void Co3lidarView::Dump(CDumpContext& dc) const
{
      CView::Dump(dc);
}

Co3lidarDoc* Co3lidarView::GetDocument() // non-debug version is inline
{
      ASSERT(m_pDocument->IsKindOf(RUNTIME_CLASS(Co3lidarDoc)));
      return (Co3lidarDoc*)m_pDocument;
}
#endif //_DEBUG

////////////////////////////////////////////////////////////////////////////
//////
// Co3lidarView message handlers

void Co3lidarView::OnCountPhotonCount()
{
     if(GetGraph()->m_bNewGraph == FALSE)
    {
    MessageBox("Open a New File before beginning a Photon Count",
               "Photon Counting",MB_OKCANCEL + MB_ICONSTOP);
    }
        else
    {
      int size;       //size of array
      int iLoop;      //loop counter
      int iResult;    //return value from dialog box


        PCDLG m_dlg1;                   //declare dialog box of type
PCDLG
        iResult = m_dlg1.DoModal();     //open dialog box

        //update view members with dialog members
        m_Range           = m_dlg1.m_Range;
        m_CountTime         = m_dlg1.m_CountTime;
      bd                = m_dlg1.GPIB_Board; //identifies IEEE card
interface
```

```
      if(iResult != IDCANCEL)       //if dialog box was not cancelled
then read data
            {
            ReadCounts();                 //read the counts data from the
4101

            Co3lidarDoc* pDoc = GetDocument();   //get pointer to
document
            pDoc->SetModifiedFlag(TRUE);
            pDoc->m_TotalCounts = m_TotalCounts;

            size = m_PhotonCounts.GetSize();     //get the size of the
array that holds counts

            //update the document array with the view array
            for(iLoop = 0; iLoop < size; iLoop++)
             {
               pDoc->m_PhotonCounts.Add(m_PhotonCounts.GetAt(iLoop));
             }
            //update graph with array of counts
            if(m_bHighCount)
             {
                GetGraph()->SetDataPoints(m_HighPhotonCounts);
             }
            else
             {
                GetGraph()->SetDataPoints(m_PhotonCounts);
             }
           }

        //reset system
        send_cmd(10,0,13);    //reset the LAM
        ibsic(bd);            //send interface clear
        ibonl(bd,0);          //place interface board offline

      Invalidate();  //trigger OnDraw function
   }
}

void Co3lidarView::OnCountSettings()
{
      SetupDlg m_dlg2;  //declare a dialog box of type SetupDlg
      m_dlg2.DoModal(); //open the dialog box

      //update data members of view class with new values
      //of the dialog box
    m_AmpType          = m_dlg2.m_AmpType;
      m_AmpGain          = m_dlg2.m_AmpGain;

    m_DiscName         = m_dlg2.m_DiscName;
      m_DiscSetting      = m_dlg2.m_DiscSetting;
      m_PulseWidth       = m_dlg2.m_PulseWidth;

      m_PMTType          = m_dlg2.m_PMTType;
      m_PMTSerialNumber = m_dlg2.m_PMTSerialNumber;
    m_PMTVoltage       = m_dlg2.m_PMTVoltage;
    m_PMTImpedance     = m_dlg2.m_PMTImpedance;
```

```
    m_PulseRate        = m_dlg2.m_PulseRate;
  m_GateOnTime       = m_dlg2.m_GateOnTime;
    m_GateDelay        = m_dlg2.m_GateDelay;

    //Get a pointer to the document
    Co3lidarDoc* pDoc = GetDocument();
    //update data members of the document with new values
    //of the view class members
  pDoc->m_AmpType          = m_AmpType;
    pDoc->m_AmpGain          = m_AmpGain;

  pDoc->m_DiscName         = m_DiscName;
    pDoc->m_DiscSetting      = m_DiscSetting;
    pDoc->m_PulseWidth       = m_PulseWidth;

  pDoc->m_PMTType          = m_PMTType;
  pDoc->m_PMTSerialNumber = m_PMTSerialNumber;
  pDoc->m_PMTVoltage       = m_PMTVoltage;
  pDoc->m_PMTImpedance     = m_PMTImpedance;

    pDoc->m_PulseRate        = m_PulseRate;
  pDoc->m_GateOnTime       = m_GateOnTime;
    pDoc->m_GateDelay        = m_GateDelay;

  Invalidate();
}

void Co3lidarView::OnGraphColor()
{
      CColorDialog dlg(GetGraph()->GetGraphColor());

      if (dlg.DoModal() == IDOK)
      {
      GetGraph()->SetGraphColor(dlg.GetColor());
      Invalidate();
      }
}

void Co3lidarView::OnGraphLine()
{
      GetGraph()->SetGraphType(CGraph::LINE);
      Invalidate();
}
void Co3lidarView::OnGraphAnistropic()
{
      GetGraph()->SetMappingMode(MM_ANISOTROPIC);
      Invalidate();
}
void Co3lidarView::OnGraphIsotropic()
{
      GetGraph()->SetMappingMode(MM_LOENGLISH);
      Invalidate();
}
void Co3lidarView::OnGraphScaling()
{
      int iResult;              //return value of dialog box
```

```
        AxisDlg m_dlg;              //declare dialog box of type AxisDlg
        iResult = m_dlg.DoModal();//open dialog

        UpdateData(TRUE);           //update axisdlg data members

        if(iResult == IDOK)
        {
          //update view data members if user pressed OK button
          m_YMax = m_dlg.m_YMax;
          GetGraph()->m_nYMaxRange = m_YMax;

          if(GetGraph()->m_bPhotonCountGraph)
            {
              if(m_bHighCount)
                {
                  GetGraph()->SetDataPoints(m_HighPhotonCounts);
                }
              else
                {
                  GetGraph()->SetDataPoints(m_PhotonCounts);
                }
            }
          Invalidate();         //trigger call to Draw Function
        }
}
void Co3lidarView::OnLButtonDblClk(UINT nFlags, CPoint point)
{
        CView::OnLButtonDblClk(nFlags, point);
        m_YMax = GetGraph()->m_nYMaxRange;
        if(m_YMax > 30)
        {
        m_YMax = m_YMax - 30;
        GetGraph()->m_nYMaxRange = m_YMax;
          Invalidate();
        }
}
void Co3lidarView::OnRButtonDblClk(UINT nFlags, CPoint point)
{
        CView::OnRButtonDblClk(nFlags, point);
        m_YMax = GetGraph()->m_nYMaxRange;
        if(m_YMax <= 32000)
        {
        m_YMax = m_YMax + 30;
        GetGraph()->m_nYMaxRange = m_YMax;
          Invalidate();
          }
}
void Co3lidarView::OnHelpDavid()
{
    double          nu_rd;
    FILE            *fr;
    int iLoop,iSize;
    iSize = m_PhotonCounts.GetSize();
    fr = fopen("pcounts2.txt","w");
    for(iLoop=0;iLoop<iSize;iLoop++)
      {
        nu_rd = m_PhotonCounts.GetAt(iLoop);
```

```
   send_cmd_dat(16, 1, 13, 001, 000, 000); //write address of first
data word
                                          // to be read from the
averaging memory
   send_cmd_dat(16, 1, 13, 001, 000, 000); //write address of first
data word
   send_cmd( 2, 0, 13);           //reads the signal averaged waveform
data

 //read the data stored in the 4101
   while(Q == 1)
     {
      read_dat2(rd);
         if((rd[3] & 0x02) == 0x00)
           {
             Q = 0;
             break;
           }

     nu_rd  = rd[0] & 0x00ff;        //read first eight bits
     temp   = rd[1] & 0x00ff;        //read second eight bits
     nu_rd += (temp << 8);           //add first and second
     temp   = rd[2] & 0x00ff;        //read last eight bits
     nu_rd += (temp << 16);          //add last to first and second

     m_PhotonCounts.Add(nu_rd); //store value into next array element
     if(nu_rd >= 32000) m_bHighCount = TRUE;
     fprintf(fp,"%d\t%.f\n", count,nu_rd);      //write count and nu_rd
to file "Russell"
     count++;                                   //number of data sweeps
     m_TotalCounts += nu_rd;                     //sum of photon events
   }
  fprintf(fp,"%.f",m_TotalCounts);
  fclose(fp);    //close the file

 // m_PhotonCounts.SetAt(0,m_PhotonCounts.GetAt(1)) ;         //veto
first bin

   if(m_bHighCount)
     {
       DivideDataby1000();
       GetGraph()->m_bHighData = TRUE;
     }
}//end of ReadData

//*****************************************************************
***********//
////////////////////////////////////////////////////////////////////
////////
//                                          ARRAY Math Functions
////////////////////////////////////////////////////////////////////
////////
void Co3lidarView::FindMaxValue(CDWordArray& m_dwArray)
{
  int iSize;
  int iLoop;
  DWORD iPresentMaxValue;
```

```
  iPresentMaxValue = 200;//
  GetGraph()->m_nYMaxRange = iPresentMaxValue;
  iSize = m_dwArray.GetSize();
  if(iSize > 0)
  {
    for(iLoop=0; iLoop < iSize; iLoop++)
      {
       if(m_dwArray.GetAt(iLoop) > 200)
         {
           iPresentMaxValue = m_dwArray.GetAt(iLoop);
           GetGraph()->m_nYMaxRange = iPresentMaxValue;
         }
      }
  }

}
void Co3lidarView::FindMaxValue2(CDWordArray& m_dwArray)
{
  int iSize;
  int iLoop;

  iSize = m_dwArray.GetSize();
  if(iSize > 0)
  {
    for(iLoop=0; iLoop < iSize; iLoop++)
      {
       if(m_dwArray.GetAt(iLoop) > 32000)
            {
            m_bHighCount = TRUE;
            GetGraph()->m_bHighData = TRUE;
            m_bTemp = TRUE;
            }
      }
   }
void Co3lidarView::DivideDataby1000()
{
  int iSize;
  int iLoop;
  iSize = m_PhotonCounts.GetSize();
  m_HighPhotonCounts.RemoveAll();
  for(iLoop = 0; iLoop < iSize; iLoop++)
    {
      m_HighPhotonCounts.Add((m_PhotonCounts.GetAt(iLoop)/1000));
    }
}
```

APPENDIX C

Summary of Photomultiplier Research conducted byBrad Eccels

Brad Eccles completed his Master of Science in Electrical Engineering at Old Dominion University in August of 1997. His research was an investigation of photomultiplier tubes for use in photon counting systems for lidar applications. The objectives were to determine the best PMT suitable for a UV DIAL system and to characterize its performance and determine the optimum conditions in which to operate the PMT for a photon counting system.

Eccles research concluded that the *ETI 9214QB #5150* was the best PMT available for a photon counting system to make UV DIAL measurements. This PMT has a high QE and gain of 31.5% @300 nm and 1.5e7@1300 VDC respectively. He also found that optimum performance in a photon counting system with this PMT requires a discriminator threshold of 110 mV and a discriminator output pulse width of 5 nsec.

The gating circuit chosen through Eccles' research is a dynode-gating scheme. When the gate signal is not applied to the circuit (see Fig. C.1), the 2^{nd}, 4th, and 6^{th} dynodes are held at the same voltage as the 1^{st}, 3^{rd}, and 5^{th} dynodes respectively. Therefore, electrons are not multiplied through the chain because no potential drop exists between each pair of dynodes. Conversely, when the gate signal is applied, a potential drop allows the multiplication of photoelectrons released from the photocathode. This gating scheme has high gain stability and hold-off ratio compared to other types of typical photomultiplier circuits [23].

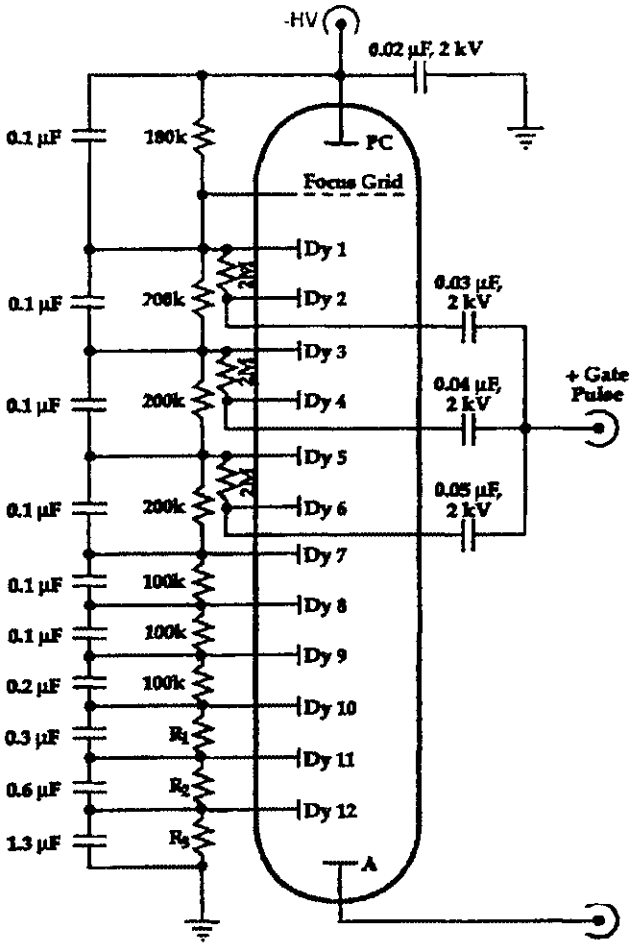

Figure C.1. Dynode Gating circuit for Photomultiplier tube.